minerals

MDPI

Article

Petrogenesis of Devonian and Permian Pegmatites in the Chinese Altay: Insights into the Closure of the Irtysh–Zaisan Ocean

Mengtao Wang [1,2,3] and Xin Zhang [1,*]

[1] School of Geography and Planning, Ningxia University, Yinchuan 750021, China; wangmengtao@mail.gyig.ac.cn
[2] Key Laboratory of High-Temperature and High-Pressure Study of the Earth's Interior, Institute of Geochemistry, Chinese Academy of Sciences, Guiyang 550002, China
[3] University of Chinese Academy of Sciences, Beijing 100049, China
* Correspondence: zhangxin869@126.com; Tel.: +86-17752401030

Abstract: Owing to tectonic, magmatic, and metamorphic controls, pegmatites associated with different spatiotemporal distributions exhibit varying mineralisation characteristics. The petrogenesis of pegmatites containing rare metals can improve the understanding of geodynamic processes in the deep subsurface. In order to understand the difference of petrogenesis between Devonian and Permian pegmatites, zircon U-Pb geochronological and Hf-O isotope analyses were performed on samples of the Jiamanhaba, Amulagong, and Tiemulete pegmatites from the Chinese Altay. According to the results obtained, the Amulagong and Tiemulete pegmatites were formed during the Devonian, and samples that were analysed yielded zircon U-Pb ages of 373.0 ± 7.8 and 360 ± 5.2 Ma, respectively. Samples from these pegmatites produced εHf(t) values of 2.87–7.39, two-stage model ages of 900–1171 Ma and $\delta^{18}O$ values of 9.55‰–15.86‰. These results suggest that the pegmatites were formed via an anatexis of mature sedimentary rocks deep in the crust. In contrast, the Jiamanhaba pegmatite was formed during the Permian, and its samples produced εHf(t) and $\delta^{18}O$ values of 2.87–4.94 and 6.05‰–7.32‰, respectively, which indicate that the associated magma contained minor amounts of mantle/juvenile materials. The petrogenesis of pegmatites containing rare metals can reveal tectonic settings of their formation. A combination of data that were generated in the present study and existing geochronological and Hf-O isotope data for felsic igneous and sedimentary rocks in the Chinese Altay shows that the εHf(t) sharply increased while the $\delta^{18}O$ suddenly decreased between Late Carboniferous and Early Permian. These changes highlight a tectonic transformation event during this critical period. This tectonic event promoted mantle–crustal interactions, and thus, it was probably linked to assemblages of the Altay orogen and the Junggar Block. The present study provides evidence that the Irtysh–Zaisan Ocean probably closed during the Late Carboniferous (~300 Ma).

Keywords: petrogenesis; zircon U-Pb dating; zircon Hf-O isotopes; the Irtysh–Zaisan Ocean

Citation: Wang, M.; Zhang, X. Petrogenesis of Devonian and Permian Pegmatites in the Chinese Altay: Insights into the Closure of the Irtysh–Zaisan Ocean. *Minerals* **2023**, *13*, 1127. https://doi.org/10.3390/min13091127

Academic Editor: Harald G. Dill

Received: 29 June 2023
Revised: 18 August 2023
Accepted: 23 August 2023
Published: 25 August 2023

1. Introduction

Granitic pegmatites (hereafter referred to as pegmatites) are igneous rocks comprising skeletal crystals or graphic zones and/or large mineral grains, and these are associated with systematic variations [1]. Pegmatites are often enriched in Li, Be, Nb, Ta, Rb, Cs, Hf, and other rare metals, and thus, these rocks are associated with several mineral deposits around the world. Prominent pegmatite-linked deposits include the following: the Keketuokay No. 3 Li-Be-Nb-Ta-Rb-Cs-Hf deposit in Xinjiang, China, Tanco Li-Ta-Cs deposit in Canada and Bikita Li deposit in Zimbabwe [2]. The distribution of pegmatites in the world and continental convergence events exhibit a strong spatiotemporal correlation, and this highlights the significance of tectonic activities on the formation of pegmatites [3–5].

Therefore, numerous studies on the petrogenesis of pegmatites have been undertaken in different parts of the world.

The classification of pegmatite is as complex as the pegmatite itself. Others classification schemes focus on the internal structure, paragenetic relationship, bulk composition, petrogenetic aspects, nature of parent medium, and geochemical features. However, all schemes ignore differences in the geological environment, which is important for understanding pegmatites. Ginsburg et al. [6] and Černy [7] proposed a new classification scheme: according to the petrogenetic of pegmatites, three classes can be distinguished here including the NYF family, LCT family, NYF + LCT family. The NYF family has a prominent accumulation of Nb, Ta, Ti, Y, Sc, REE, Zr, U, Th and F (Nb > Ta). The parent granites are mainly subaluminous to metaluminous A- to I-types, which are correlated with anorogenic setting [8,9]. The LCT family is enriched in Li, Rb, Cs, Be, Sn, Ta, Nb (Ta > Nb), B, P and F. The parent granites are mainly midly to peraluminous S-, I-type which are usually strongly fractionated within individual bodies [10,11]. They are correlated with orogenic setting (syn-orogenic and post-orogenic) [8,9]. The NYF + LCT family pegmatites display mixed geochemical and mineralogical characteristics [12]. Jiamanhaba, Amulagong, Tiemulete—the three pegmatites we studied—are all the LCT-type. Two petrogenetic models have been advanced regarding pegmatites, and based on the genetic relationship between LCT-type pegmatites and S-type granites, Černy and Meintzer [10], Černý [8] and Selway et al. [13] indicated that pegmatites represent consolidation products of residual magmas from the late fractional crystallisation of granitic magmas. The J-B model was proposed by Jahns and Burnham [14] based on the experimental data. They considered water-saturated magma playing a very important role in the forming of internal zoning (in response to fractional crystallisation) in pegmatite. The coarse grain texture is ascribed to the effects of the rapid transfer of materials. Supercritical fluids, which contain H_2O and volatiles, are crucial for the transportation of materials that promote the crystallisation of minerals. Therefore, large crystals usually form in the fluid phase, whereas small crystals develop directly from the silicate melt. In contrast, London et al. [15,16] and London [17] proposed the London model, in which pegmatite formation was associated with low H_2O contents of granitic magmas. The zonations in pegmatites were attributed to the presence of boundary layers, where volatiles and incompatible elements cause crystallisation from the exterior to the interior. Furthermore, based on experimental studies and the observation of miarolitic cavities in pegmatites, a high content of H_2O was indicated to inhibit the growth rate of crystals, and this accounts for the absence of large crystals. According to another model, the petrogenesis of pegmatites is related to partial melting deep in the crust instead of the fractional crystallisation of granitic magmas [18–22]. In fact, a genetic relationship between pegmatites and granites is commonly lacking. The Tanco (Canada), Greenbush (Australia) and Keketuokay No. 3 (China) pegmatites exhibit no genetic relationship with the host granites. However, previous studies suggest that pegmatites are commonly associated with anatexis [21–30].

The Altay Orogenic Belt in the north of the Xinjiang Uygur Autonomous Region is an important component of the Central Asian Orogenic Belt (CAOB) [31–40] (Figure 1). In this prominent metallogenic belt, more than 100,000 pegmatite veins are distributed across 38 fields [41–43]. These rare metal-rich pegmatite veins are primarily associated with Permian and Triassic Periods. Among these fields, major deposits include the following: super large Li-Be-Ta-Nb-Cs in the Keketuohai No. 3, super large Li in Kaluan 650, 805, 806, and 807, large Li-Be-Nb-Ta in Kelumute No. 112, small Be-Li-Nb-Ta in Xiaokalasu, small Be-Nb-Ta Dakalasu and Yelaman, and small Be in Jiamanhaba pegmatites [44–51]. Relatedly, Devonian and Carboniferous rare metal deposits include the following: small Li-Be-Ta-Nb deposit in Amulagong and small Li-Be-Ta-Nb-Cs deposit in Talati pegmatites [23]. Previous studies on the pegmatites in Chinese Altay mainly focus on the chronology of the pegmatites and the geochemical evolution of the magma. The main dating methods used in the Institute of Chronology are muscovite Ar-Ar dating [42,52–54], zircon U-Pb dating [21,45,46,49–51,53–59], and niobium-tantalum U-Pb dating, which has appeared in

recent years [48,54]. Because muscovite is easily disturbed by magmatic hydrothermal, the dating results of muscovite are quite different from those of zircon and niobium-tantalite. The petrogenesis of pegmatite in Chinese Altay has always been controversial. Predecessors have speculated that pegmatite may be the product of the late evolution of granite batholith, but no clear evidence has been presented to prove the genetic evolution relationship between the two. In the present study, Hf and O isotope data were utilised to evaluate source and tectonic setting differences between the Permian Jiamanhaba pegmatite and Devonian Amulagong and Tiemulete pegmatites which show different distribution, quantity and mineralisation of them during two periods.

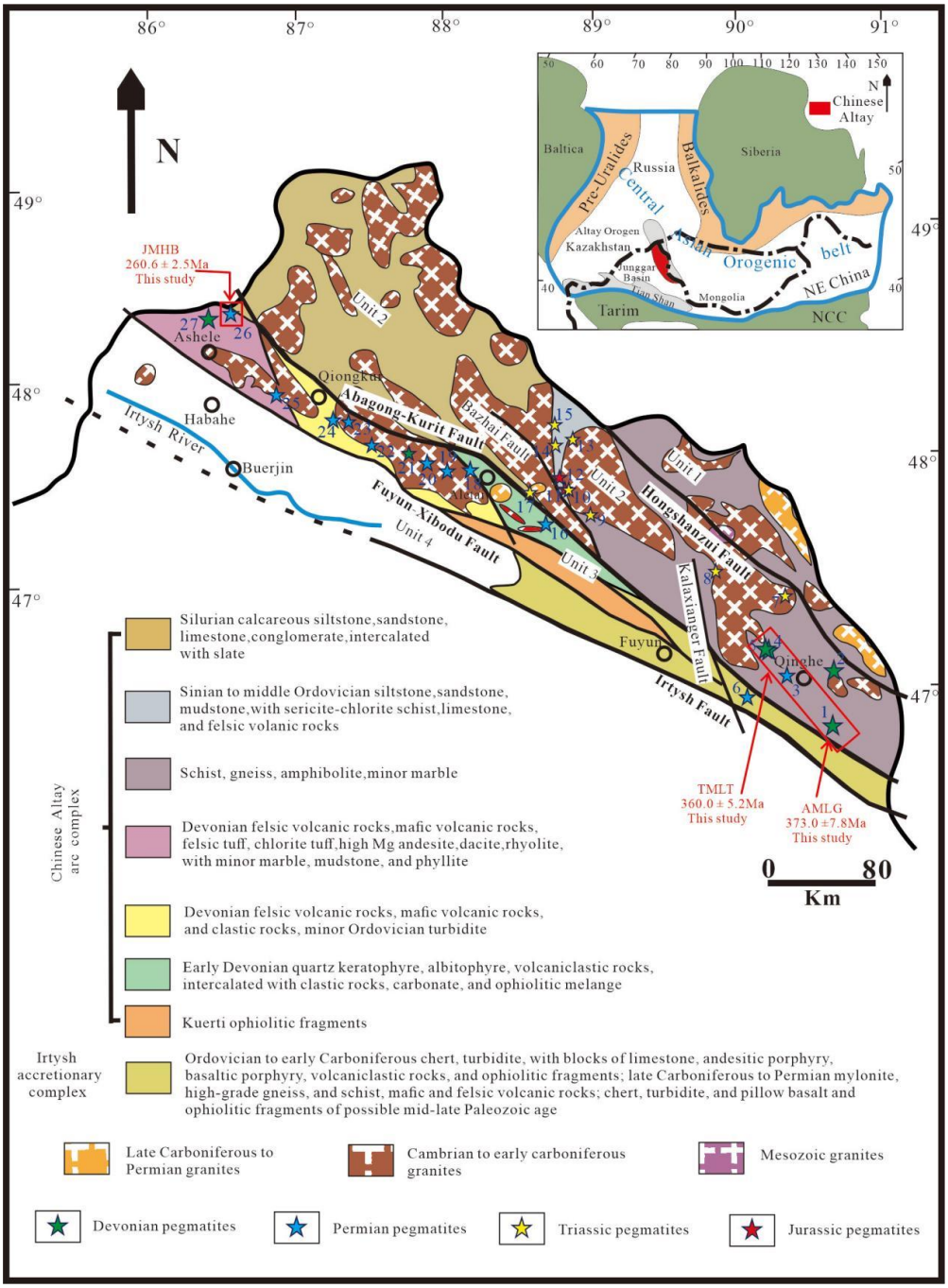

Figure 1. Geological map of the Chinese Altay (modified after Xiao et al. [60]; Cai et al. [61,62]; Xiao and Santosh, [63]; the age data are from Zhang et al. [21]; Lv et al. [22,23,50]; Wang et al. [45]; Chen, [46]; Ma et al. [49]; Ren et al. [51]; Wang et al. [64]). The age data of pegmatites are shown in Table 1.

Table 1. The age of pegmatites in Chinese Altay.

Number	Pegmatite Deposit	Mineralisation Type	Position	Scale	Method	Age (Ma)	Reference
1	Amulagong	Li-Be-Ta-Nb	Unit 3	small	LA-ICP-MS	373.0 ± 7.8	this study
						358	[23]
2	Talati	P-Cs-Nb-Be-Li	Unit 3	small	LA-ICP-MS	386	[23]
3	Baicheng	Li-Be-Ta-Nb	Unit 3	small	LA-ICP-MS	274	[22]
4	Tiemulete1	(F)-Nb-P-B-Be	Unit 3	small	LA-ICP-MS	333	[23]
5	Tiemulete2	Mica-Be	Unit 3	small	LA-ICP-MS	360.0 ± 5.2	this study
6	Bulukete	Be	Unit 3	small	LA-ICP-MS	275.5 ± 4.2	[51]
7	Asikaerte	Be-Nb-Mu	Unit 2	large	LA-ICP-MS	229.0 ± 3.0	[56]
8	Kokotokay No. 3	Li-Be-Ta-Nb-Cs-Rb-Hf	Unit 2	super large	LA-ICP-MS	208.1 ± 0.8	[51]
					LA-ICP-MS	212.7 ± 0.5	[51]
					LA-ICP-MS	220	[45]
					LA-ICP-MS	220–209	[46]
					LA-ICP-MS	190.6 ± 1.2	[51]
					LA-ICP-MS	214.9 ± 2.1	[51]
					LA-ICP-MS	180.7 ± 0.5	[51]
9	Husite	Be-Nb-Ta	Unit 2	middle	LA-ICP-MS	244.3 ± 1.1	[51]
10	Qunku	Be-Nb-Ta	Unit 2	small	LA-ICP-MS	206.8 ± 1.6	[51]
11	Azubai 01	Be-Nb-Ta	Unit 2	middle	LA-ICP-MS	191.6 ± 2.0	[21]
12	Jiamukai	Li-Be-Ta-Nb-Cs	Unit 2	middle	LA-ICP-MS	212.2 ± 1.7	[51]
						192.0 ± 2.3	[21]
13	Kelumute	Li-Be-Nb-Ta	Unit 2	large	LA-ICP-MS	202.9 ± 0.8	[51]
						238.3 ± 2.0	[50]
14	Kaluan	Li-Nb-Ta	Unit 2	super large	LA-ICP-MS	223.7 ± 1.8	[49]
						221 ± 15	[49]
						216 ± 2.6	[49]
						224.6 ± 2.3	[21]
15	Kukalagai	Li-Nb-Ta	Unit 2	super large	LA-ICP-MS	211.3 ± 2.4	[49]
16	Dakalasu	Be-Nb-Ta	Unit 3	small	LA-ICP-MS	270.1 ± 1.7	[51]
						272.5 ± 1.4	[51]
						263.7 ± 4.4	[64]
						258	[22]
17	Hulugong	Be-Nb-Ta	Unit 2	small	LA-ICP-MS	246.8 ± 1.2	[51]
18	Xiaokalasu	Be-Li-Nb-Ta	Unit 3	small	LA-ICP-MS	267.5 ± 3.5	[64]
19	Qiemuerqieke	REE	Unit 3	small	LA-ICP-MS	253	[22]
20	Taerlang	Be-Nb-Ta-REE	Unit 3	small	LA-ICP-MS	256	[22]
21	Qiebielin	Nb-P-B-Be	Unit 3	small	LA-ICP-MS	403	[23]
22	Akebasitawu	Be-Nb-Ta-REE	Unit 3	small	LA-ICP-MS	249.7 ± 0.7	[51]
						253	[22]
23	Saerjiake	Li-Be-Ta-Nb	Unit 3	small	LA-ICP-MS	253	[22]
24	Hailiutan	REE	Unit 3	small	LA-ICP-MS	254	[22]

Table 1. *Cont.*

Number	Pegmatite Deposit	Mineralisation Type	Position	Scale	Method	Age (Ma)	Reference
25	Yelaman	Be-Nb-Ta	Unit 3	small	LA-ICP-MS	267.8 ± 1.4	[51]
						262.8 ± 3.1	[64]
						263	[22]
26	Jiamanhaba	Be-Ta-Nb	Unit 3	small	LA-ICP-MS	269.4 ± 1.6	[51]
						260.6 ± 2.5	this study
						260	[22]
27	Jiamanhaba02	Nb-P-B-Be	Unit 3	small	LA-ICP-MS	395	[23]

2. Geological Setting

2.1. Regional Geology

The Chinese Altay Orogenic Zone extends from Mongolia in the east to Kazakhstan and Russia in the west. It is situated between the South Siberian Craton in the north and the Junggar Block in the south. The Chinese Altay was partitioned into four terranes by the Hongshanzui–Nort, Kurti–Abagong, Fuyun–Xibodu and Irtysh faults [32,42,45,61,62,65]. The North Altay Terrane (Unit 1) is bounded in the south by the Hongshanzui–Nuoerte fault [32,66], and it contains mainly clastic sediments (shales, siltstones, greywackes, and sandstones), limestones, granites, and minor greenschist facies island-arc metavolcanic rocks that were formed in the Late Devonian to Early Carboniferous [67–69]. The Central Altay Terrane (Unit 2) is sandwiched between the Hongshanzui–Nuoerte fault in the north and the Kurti–Abagong fault in the south [31,32]. This terrane contains mainly metamorphosed sedimentary rocks, early to middle Paleozoic granites [33,38,39,49,61,62,66,69–73] and volcanic rocks (Habahe Group). In this terrane, granite commonly occurs as intrusions into sedimentary rocks, and this indicates frequent magmatism. Relatedly, the Qiongkuer Terrane (Unit 3) is sandwiched between the Kurti–Abagong fault in the north and the Fuyun–Xibodu fault in the south. It comprises the Silurian Kulumuti Group and Early Devonian Kangbutiebao and Middle-Late Devonian Altay formations [32,74], and these strata are coveal with exposed granites [38,66,70–72,75–78]. Lastly, the South Altay Terrane (Unit 4) is sandwiched between the Fuyun–Xibodu fault in the north and the Irtysh fault in the south. The northwestern part is composed by sediments. The southeastern part contains mainly Devonian fossil-bearing sedimentary rocks (Kangbutiebao Formation) and the overlain Carboniferous Formations. In addition, a few Carboniferous–Permian volcaniclastic rocks are exposed in this area [32,74,79].

Geochronology data show that granitic intrusions were common in the Chinese Altay from the Early Palaeozic to the Early Mesozoic, and these attained a peak in the Devonian [35,37,38,44,50,51,61,62,72,80–84]. The Palaeozoic granites, which are dominantly I- and S-types, are widely distributed in the Central Altay Terrane [61,85]. The peak of granitic magmatism in the Permian was coeval with pegmatites and pyrometamorphism [21,50,51,70,77,78,80,86]. The Permian granites involve I, A, I-A, and I-S types, and these are common across the Qiongkuer Terrane [78,87–89]. In the Chinese Altay, pegmatites are dominantly found in the Central Altay and the Qiongkuer terranes. The over 100,000 pegmatite veins, which are distributed in 38 fields, occur mainly in the Halong–Qinghe and Jiamanhaba–Dakalasu metallogenic subzones. Owing to tectonic, magmatic, and metamorphic controls, pegmatites associated with different spatiotemporal distributions show varying mineralisation characteristics. Devonian–Carboniferous pegmatites are concentrated in the Halong–Qinghe subzone, whereas Permian pegmatites are abundant in the Jiamanhaba–Dakalasu subzone in the Qiongkuer Terrane. Triassic pegmatites occur in both the Qiongkuer and the Central Altay terranes, whereas most Jurassic pegmatites are found in the Central Altay Terrane, with subordinate occurrences in the North Altay

Terrane. Minerals that are common in the Permian and Devonian–Early Carboniferous pegmatites in the Qiongkuer Terrane include the following types: Be, Nb, Ta, and Li. Minerals and mineral assemblages that are dominant in Triassic pegmatites in the Qiongkuer and the Central Altay terranes are the following types: Be, Li-Nb-Ta, Li-Be-Nb-Ta, and Be-Li-Nb-Ta (-Cs-Rb-Hf).

2.2. Geology of the Jiamanhaba, Tiemulete and Amulagong Pegmatites

2.2.1. Jiamanhaba Pegmatite

The Jiamanhaba pegmatite field is in the northwest of the Chinese Altay, approximately 50 km from Habahe County in the south and just 10 km from the border between China and Kazakhstan in the west [51]. It is in the west terminal of the Jiamanhaba–Dakalasu metallogenic subzone in the Qiongkuer Terrane, which belongs to the west region of the Kabaer–Xibodu magmatic arc. These pegmatites are associated with many intrusive rocks in the area, including biotite granites and Caledonian plagiogranites. In the south of the field, minor outcrops of Late Variscan two-mica granites are also found. Pegmatites are scattered around this field, and these are characterised by lengths of <500 m and widths of <10 m. These pegmatites exhibit a low degree of fractionation, simple zonation, and common Be mineralisation.

The Jiamanhaba pegmatite is hosted in biotite granites, and based on outcrops that measure 50 m in length and 7 m in width, it is associated with an ESE strike of 98° and a dip of 20°. Across the upper to the lower section, the pegmatite vein can be divided into the following internal zones: graphic, saccharoidal albite, massive microcline, and quartz–muscovite nested. Major minerals in the Jiamanhaba pegmatite are muscovite, microcline, quartz, and albite, whereas spessartite, apatite, tourmaline, and zircon are dominant accessory minerals. Prominent rare metal minerals in this pegmatite are beryl and columbite-tantalite. The Be mineralisation is abundant in the graphic and massive microcline texture zones.

2.2.2. Amulagong Pegmatite

The Amulagong pegmatite field is in the southeast of the Chinese Altay, approximately 35 km from Qinghe County in the east. It occurs between the Mieriteke and Baleqige–Keketuomusike faults, and this field was intruded by numerous Variscan porphyritic biotite granites (strike = WNW 315°) that contain medium-coarse crystals. Variscan diorites (strike = WNW 350°) are also scattered in the north and south of the Nuogan River over a length and a width of 3.9 and 1.4 km, respectively. The 116 pegmatite veins in this field cover an area of >3 km^2, and these veins, which intruded diorites along fissures, display a NW strike and dip of 45°. The majority of these veins are <100 m long, whereas some are >200 m long, but all are <20 m wide. Several pegmatite veins are characterised by low Be and Be-Nb-Ta mineralisation, whereas others show high Be-Li-Nb-Ta mineralisation.

The studied Amulagong pegmatite is hosted in medium Variscan diorites, and it is characterised by a length of approximately 70 m and an average width of 8 m. Across the upper to the lower section, pegmatite veins can be partitioned into the following zones: graphic, saccharoidal albite, massive microcline, quartz–muscovite nested, and cleavelandite albite. Major minerals in this pegmatite are muscovite, microcline, quartz, and albite, whereas spessartite, apatite, tourmaline, and zircon constitute accessory minerals. Ore minerals in this deposit are beryl, columbite–tantalite, spodumene, and pollux. Beryllium mineralisation is concentrated in the massive microcline and quartz–muscovite nested zones. Conversely, Nb and Ta are hosted in manganotantalites mainly in the massive microcline zone, whereas spodumene crystallised in both the massive microcline and cleavelandite albite zones.

2.2.3. Tiemulete Pegmatite

This pegmatite in the southeast of the Chinese Altay is approximately 25 km from Qinghe County in the southeast. It is within the Qinghe pegmatite ores area in the

Qiongkuer Terrane, which represents the core of the Buleke Anticline. Few muscovite- and beryl-bearing pegmatites intrude the medium-sized Early Variscan diorite body with an east–west strike located east of the pegmatite field. In the pegmatite field, strata involve those of the Early–Middle Ordovician Habahe Formation, including garnet biotite gneisses, sillimanite–two mica gneisses, augen gneisses, striped, enterolithic and augen migmatites, as well as biotite–plagioclase gneisses, which exhibit a strike of 130° and dip of 40° [23]. In the west of this field, 40 muscovite-bearing pegmatite veins occur as intrusions, and 28 of these contain rare metals. These veins are scattered across the field, and most are <200 m long and <5 m wide.

The Tiemulete pegmatite is hosted in biotite–plagioclase and plagioclase hornblende gneisses, and it measures 190 m in length and 2.21 m in width, with a strike of WNW 330° and a dip of 78°. The veins are shallow and exhibit characteristics of expansion and contraction. Across the upper to the lower section, the pegmatite vein can be divided into the following zones: graphic, saccharoidal albite, massive microcline, and quartz–muscovite nested. The quartz–muscovite nested zone is characterised by a random mixture of smoky grey quartz and scaly muscovite. Major minerals in this pegmatite are muscovite, microcline, quartz, and albite, whereas spessartite, apatite, tourmaline, and zircon are accessory minerals. Ore minerals in this deposit include beryl and columbite–tantalite. The Be mineralisation is concentrated in the saccharoidal albite zone, and the beryl crystals are small and dispersed. Muscovite is abundant in the quartz–muscovite nested zone, but this is non-uniformly distributed in the pegmatite vein.

2.3. Materials

Jiamanhaba pegmatite can be divided into four mineral assemblage zones: graphic assemblage; saccharoidal albite assemblage; massive microcline assemblage and nested quartz–muscovite assemblage. Graphic assemblage is composed of quartz (40%), potassium feldspar (40%) and muscovite (20%). It is located in the upper wall of the gently inclined pegmatite vein and accounts for 10% of the total volume of the whole vein (Figure 2a). The saccharoidal albite assemblage is mainly composed of quartz (45%) and albite (55%), accounting for 10% of the total volume of the whole vein (Figure 2a,c). The massive microcline assemblage is mainly composed of block microcline (98%) and muscovite (2%), accounting for 40% of the total volume of the whole vein. The nested quartz–muscovite assemblage is mainly composed of quartz (30%), albite (50%) and muscovite (20%), accounting for 40% of the total volume of the whole vein (Figure 2b).

Amulagong pegmatite can be divided into five mineral assemblage zones: graphic assemblage; saccharoidal albite assemblage; massive microcline assemblage; nested quartz–muscovite assemblage and cleavelandite albite–spodumene assemblage. The graphic assemblage is located on the edge of the upper wall of the inclined pegmatite vein, consisting of medium coarse-grained quartz (40%) and potassium feldspar (60%), with rare metal mineralisation. It accounts for 20% of the total volume of the whole vein (Figure 2e). The saccharoidal albite assemblage consists of fine-grained quartz (30%) and albite (70%), accounting for 30% of the total vein volume (Figure 2d,f). The massive microcline assemblage is mainly composed of microcline (60%), quartz (30%) and muscovite (10%). Niobium–tantalite crystals in the shape of chicken feet can be seen in albitisation rocks, which accounts for 20% of the total volume of the whole vein. The nested quartz–muscovite assemblage, located in the dike footwall, about 0.5 m thick. It is mainly composed of quartz (30%), albite (40%) and muscovite (30%). It accounts for 10% of the total volume of the whole vein. The cleavelandite albite–spodumene assemblage consists mainly of foliated albite (60%), spodumene (20%) and muscovite (20%). It accounts for 20% of the total volume of the whole vein.

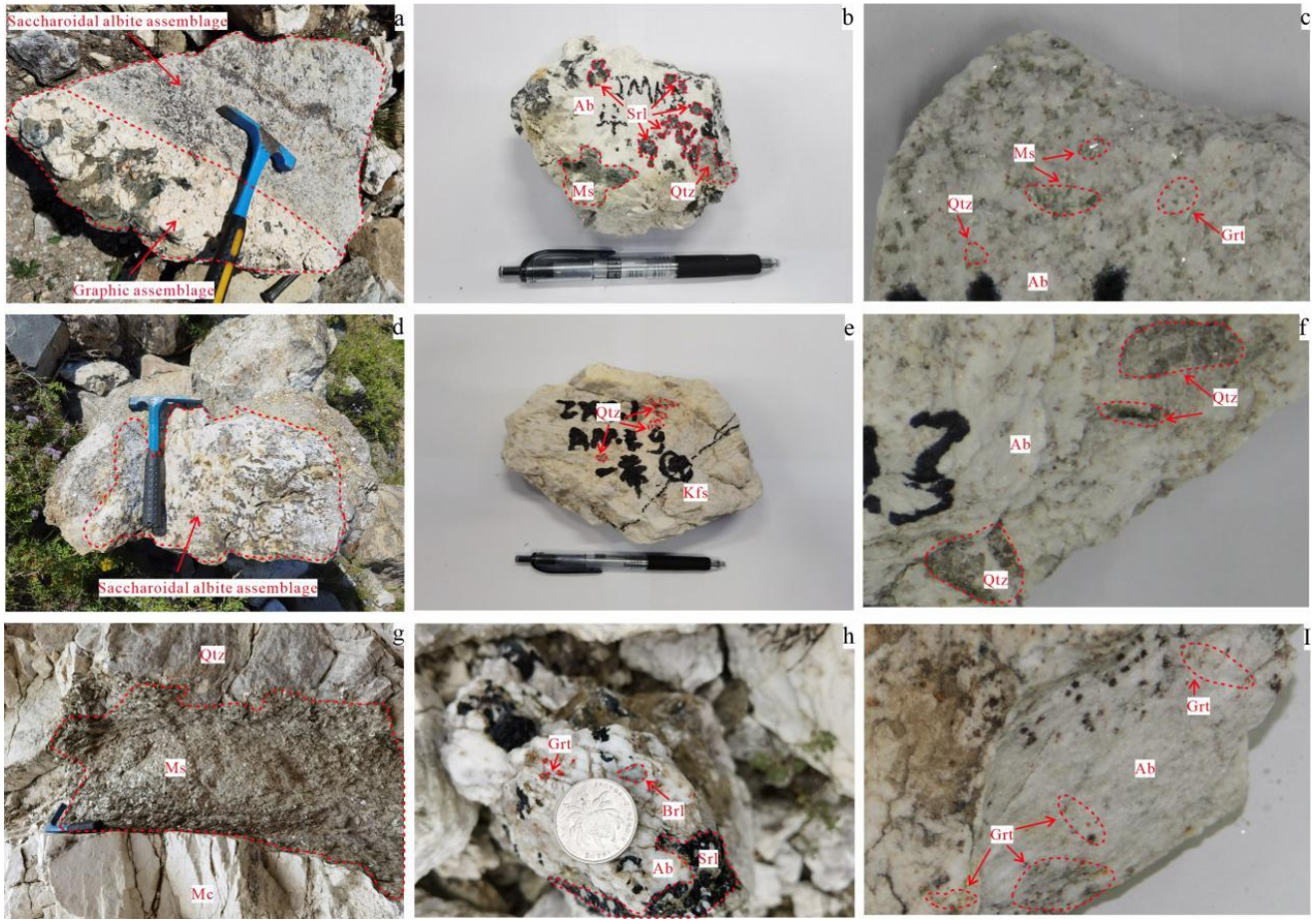

Figure 2. Photographs of the field outcrops and hand specimens of the Jiamanhaba pegmatite, Amulagong pegmatite, Tiemulete pegmatite: (**a**) contact relationship between the graphic assemblage and saccharoidal albite assemblage of Jiamanhaba pegmatite; (**b**) mineral assemblage of the nested quartz–muscovite zone of the Jiamanhaba pegmatite; (**c**) mineral assemblage of the saccharoidal albite zone of the Jiamanhaba pegmatite. (**d**) contact relationship between the saccharoidal albite assemblage and massive microcline assemblage of Amulagong pegmatite; (**e**) mineral assemblage of the graphic zone of the Amulagong pegmatite; (**f**) mineral assemblage of the saccharoidal albite zone of the Amulagong pegmatite. (**g**) contact relationship between the Muscovite ore and the wall rocks of the Tiemulete pegmatite; (**h**) mineral assemblage of the graphic zone of the Tiemulete pegmatite. (**i**) mineral assemblage of the saccharoidal albite zone of the Tiemulete pegmatite. Abbreviations: Ab, albite; Brl, beryl; Kfs, K-feldspar; Ms, muscovite; Qtz, quartz; Scl, schorl; Mc, microcline; Grt, garnet.

The Tiemulete pegmatite can be divided into four mineral assemblage zones: graphic assemblage; saccharoidal albite assemblage; massive microcline assemblage and nested quartz–muscovite assemblage. The graphic assemblage, located in the upper wall of the gently inclined pegmatite vein, is mainly composed of feldspar (80%), quartz (16%) and muscovite (4%), with beryl crystals. It accounts for 30% of the total volume of the whole vein (Figure 2h). The saccharoidal albite assemblage is mainly composed of albite (70%), quartz (27%) and muscovite (3%). It accounts for 10% of the total volume of the whole vein (Figure 2i). The massive microcline assemblage is mainly composed of feldspar (80%), quartz (13%) and muscovite (7%). It accounts for 20% of the total volume of the whole vein. The nested quartz–muscovite assemblage is an irregularly shaped aggregate of quartz (20%) and muscovite (80%). The colour of mica is brown, white, light green, and it is in the form of a wedge, plate, laminated composite. It accounts for 40% of the total volume of the whole vein (Figure 2g).

3. Methods

We distinguish the mineral assemblage zoning and production sequence of each pegmatite, and we identify the graphic assemblage as the first sequence mineral assemblage. Rocks with a fresh structural plane of graphic mineral assemblage in pegmatite are taken as samples. The contact zone between pegmatite and country rock often develops UST, which is mainly composed of potassium feldspar, tourmaline and muscovite-oriented growth perpendicular to the contact zone, and the crystal particles are fine. The saccharoidal albite assemblage located in the inner side of graphic assemblage presents transitional contact with the graphic assemblage. Since the genetics of the saccharoidal albite assemblage are not clear, samples from the middle of the graphic assemblage are taken to avoid the change of minerals and lithology in the rocks located in the inner and outer parts of the graphic assemblage. In order to ensure the selection of enough zircon grains, the weight of the sample is >10 kg.

Zircon targeting and cathodoluminescence (CL) imaging were performed in the State Key Laboratory of Mineral Deposit Geochemistry, Institute of Geochemistry, Chinese Academy of Sciences. Samples were pulverised and zircon grains were selected in a pollution-free environment. Zircons were selected through magnetic separation and flotation, and these were then sequentially pasted to target sites using epoxy resin. A scanning electron microscope was used to produce cathodoluminescence images for subsequent zircon U-Pb geochronology and Hf and O isotope measurements.

In situ zircon U-Pb isotope analysis was performed using an NWR193 laser ablation microprobe (Elemental Scientific Lasers LLC) that was attached to an Analytikjena M90 ICP-MS in the LA-ICP-MS laboratory of the State Key Laboratory of Mineral Deposit Geochemistry, Institute of Geochemistry, Chinese Academy of Sciences. Helium was used as a compensation gas to adjust the sensitivity of the laser ablation system before entry into the ICP-MS. The energy density of the ultraviolet beam that was generated by the laser was 10 J/cm^2, whereas the beam spot diameter was 30 μm. The time-resolved analysis for each sample involved durations of approximately 20–30 and 40 s for the blank and sample signals, respectively. The U-Pb data were corrected for isotope fractionation using zircon 91500 as an external standard [90,91]. Ten points in each sample were analysed in duplicate, and a point for Plesovice was used as the monitor. The NIST SRM 610 and Si were correspondingly used as internal and external standards to correct the Pb concentration. The instrument drift sensitivity calibration and calculation of element concentrations and U-Th-Pb isotope ratios were achieved using offline processing software. The Isoplot 3 offline software was used to calculate the weighted average ages and to plot these ages in the Concordia diagram [90,92,93]. The common Pb adjustment was conducted using Andersen's software [94].

The zircon Hf isotope analysis was also performed in situ using the NWR193 laser-ablation microprobe (Coherent GMBH) attached to a Neptune multicollector ICP-MS in the LA-ICP-MS laboratory of the State Key Laboratory of Mineral Deposit Geochemistry, Institute of Geochemistry, Chinese Academy of Sciences. The laser beam diameter was 32 μm and the beam energy was 10 J/cm^2. Helium was used as the carrier gas, and it was mixed with argon using a Y-shaped transfer interface. The gas mixture then transported the laser-denudated sample to the mass spectrometer for analysis. To correct for interferences of ^{176}Lu and ^{176}Y on ^{176}Hf, the ^{176}Lu/^{175} Lu = 0.02658 and ^{176}Yb/^{173}Yb = 0.796218 ratios were determined [95]. Analysis of the zircon 91500 and Plesovice standards was interspersed with that of samples to monitor the stability of the instrument. The initial ^{176}Hf/^{177}Hf ratios (εHf(t)) were calculated using the chondritic uniform reservoir (CHUR) that was proposed by Blichert-Toft and Albarede [96] as the reference. The T_{DM1} of Hf was calculated based on the depleted mantle, which involves present-day ^{176}Hf/^{177}Hf and ^{176}Lu/^{177}Hf ratios correspondingly of 0.28325 and 0.0384 [97].

A CAMECA IMS 1280-HR secondary ion mass spectrometer (France) was used for in situ zircon O isotope analysis in the State Key Laboratory of Isotope Geochemistry, Guangzhou Institute of Geochemistry, Chinese Academy of Sciences. A primary beam of

Cs^+ involving an impact potential of 10 kV and a beam current of 7 nA was spread over 10 μm^2 to generate a homogeneous beam density. A normal-incidence electron flood gun was used to compensate for the charging of samples during the analyses, while negative secondary ions were extracted using a 10 kV electric field. The O isotope analysis was conducted based on the multicollector technique using two Faraday cups [98]. Isotopic ratios of elements that are determined using the ion microprobe are often impacted by drift. The instrumental mass fractionation (IMF) between light and heavy ions is the ratio of measured to real values [99,100]. In the present study, the IMF correction was performed using the 91500 zircon standard, which is assigned a $\delta^{18}O$ value of 9.9‰ [101].

4. Results

4.1. Zircon U-Pb Dating

4.1.1. Jiamanhaba Pegmatite

Approximately 60 zircon grains measuring 50–200 μm in length were selected from Jiamanhaba pegmatite samples, and 30 were analysed. Data for a representative subset of all the zircons analysed are shown in Figure 3a. Most of the zircons analysed were short, columnar, and euhedral, and these produced aspect ratios varying from 2:3 to 3:4, whereas subordinate elongated grains yielded aspect ratios ranging from 1:2 to 1:3. The zircons that were analysed produced dark to almost black CL images (Figure 3a), but these also exhibited abundant spots and alteration zones.

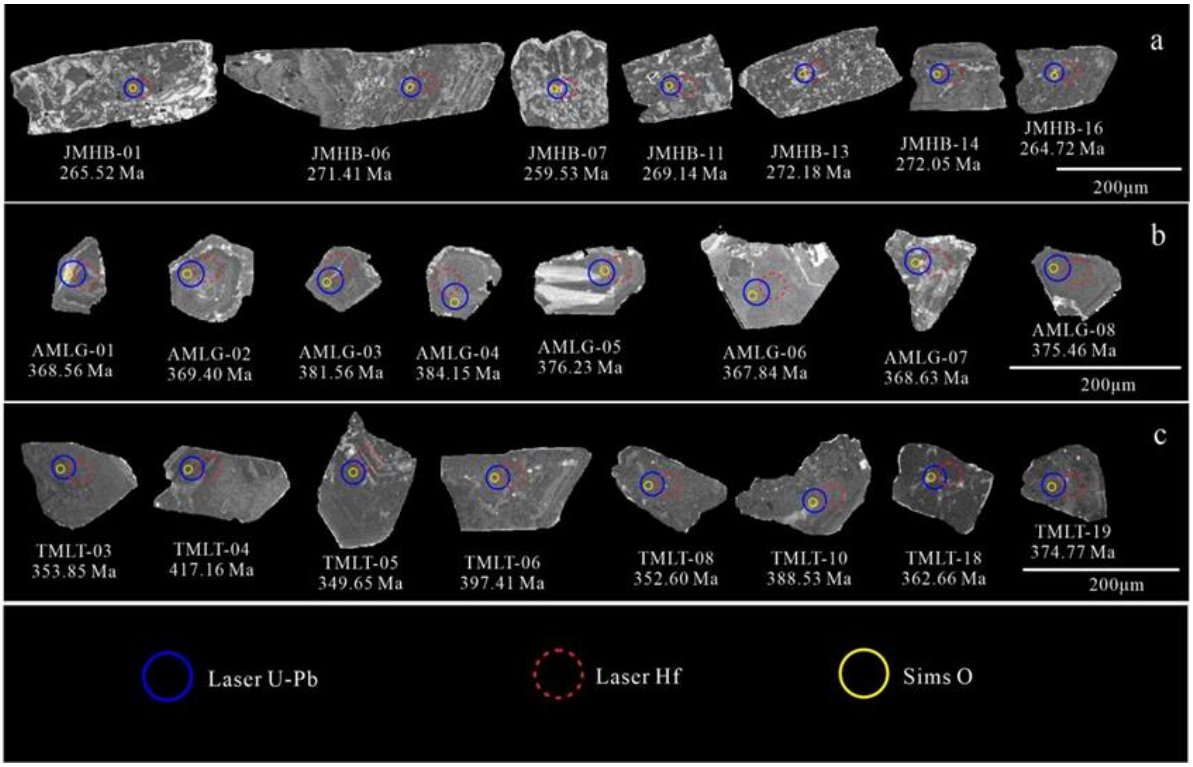

Figure 3. Zircon cathodoluminescence images of the Jiamanhaba, Amulagong and Tiemulete pegmatites. (**a**) Cathodoluminescence images of zircon grains from Jimanhaba pegmatite and their ablation locations; (**b**) Cathodoluminescence images of zircon grains from Amulagong pegmatite and their ablation locations; (**c**) Cathodoluminescence images of zircon grains from Tiemulete pegmatite and their ablation locations.

Among the 30 zircons that were analysed for U-Pb isotopes, the concentrations of Th and U for the zircon grains that were analysed ranged from 106.64 to 1851.54 and 77.86 to 6619.34 ppm, respectively, and these yielded Th/U ratios that vary from 0.035 to 1.37, whereas the $^{206}Pb/^{238}U$ ages range from 191 to 422 Ma. Sixteen yielded $^{206}Pb/^{238}U$ ages

that vary from 191 to 422 Ma, which obviously deviate from the concordant line. These results suggest that because of their high Th/U of 0.07–1.37 (Table 2), the samples were likely xenocrysts, whereas the other 14 samples, which produced an average weighted age of 260.6 ± 2.5 Ma, probably reflect the age of emplacement of the Jiamanhaba pegmatite (Figure 4a).

Table 2. The zircon U–Pb dating results of the Jiamanhaba pegmatite, the Amulagong pegmatite, and the Tiemulete pegmatite, determined by LA-ICP-MS.

Sample	Pb	Th	U	$^{207}Pb/^{206}Pb$		$^{206}Pb/^{238}U$		$^{238}U/^{232}Th$	$^{206}Pb/^{238}U$		Concordance	Th/U
	ppm	ppm	ppm	Ratio	1 Sigma	Ratio	1 Sigma	Ratio	Age (Ma)	1 Sigma		
Jiamanhaba 01	183.99	346.06	4348.64	0.057361	0.001638	0.042048	0.000735	12.825747	266	4.55	89%	0.080
Jiamanhaba 02	63.78	121.82	1552.95	0.052802	0.001812	0.040358	0.000557	13.239468	255	3.45	97%	0.078
Jiamanhaba 03	116.29	173.67	2616.00	0.062280	0.001717	0.042801	0.000698	15.654055	270	4.32	83%	0.066
Jiamanhaba 04	93.60	267.74	1999.70	0.068614	0.002253	0.044488	0.000866	7.574216	281	5.34	75%	0.134
Jiamanhaba 05	109.54	188.73	2197.48	0.080826	0.004052	0.045201	0.000879	12.989826	285	5.42	65%	0.086
Jiamanhaba 06	112.22	1851.54	2221.95	0.095521	0.002978	0.043001	0.000630	2.312056	271	3.90	48%	0.833
Jiamanhaba 07	102.10	114.38	2499.22	0.051724	0.001511	0.041081	0.000686	22.546406	260	4.25	99%	0.046
Jiamanhaba 08	156.34	631.29	3001.38	0.128373	0.003875	0.039502	0.000562	4.944176	250	3.49	26%	0.210
Jiamanhaba 09	127.71	1356.84	2788.61	0.081997	0.002592	0.041318	0.000862	2.109520	261	5.34	60%	0.487
Jiamanhaba 10	124.62	197.33	2724.45	0.065753	0.002145	0.043838	0.001020	14.085445	277	6.30	78%	0.072
Jiamanhaba 11	170.92	369.89	3724.09	0.071823	0.002019	0.042634	0.000757	10.290779	269	4.68	72%	0.099
Jiamanhaba 12	128.46	715.75	3212.64	0.126546	0.007357	0.032398	0.000987	5.282133	206	6.16	29%	0.223
Jiamanhaba 13	200.14	333.14	4261.21	0.078899	0.001743	0.043126	0.000639	13.280314	272	3.95	64%	0.078
Jiamanhaba 14	110.68	269.43	2258.75	0.088961	0.004326	0.043104	0.000804	8.872965	272	4.97	52%	0.119
Jiamanhaba 15	170.81	918.64	3848.93	0.084320	0.001868	0.040264	0.000740	5.836801	254	4.59	58%	0.239
Jiamanhaba 16	122.76	217.49	2864.89	0.058676	0.001283	0.041919	0.000550	13.835594	265	3.41	88%	0.076
Jiamanhaba 17	179.89	517.26	3929.58	0.070328	0.001989	0.043096	0.000679	9.016384	272	4.20	72%	0.132
Jiamanhaba 18	123.40	520.78	2920.75	0.065649	0.001453	0.039962	0.000747	5.902105	253	4.63	78%	0.178
Jiamanhaba 19	184.86	564.75	3334.16	0.163997	0.008366	0.037974	0.000658	6.026068	240	4.09	8%	0.169
Jiamanhaba 20	122.68	766.15	2529.16	0.091700	0.002380	0.041449	0.000684	3.807381	262	4.24	52%	0.303
Jiamanhaba 21	122.33	365.77	2737.11	0.065215	0.001683	0.041792	0.000563	7.643289	264	3.49	79%	0.134
Jiamanhaba 22	230.68	538.50	5199.49	0.060367	0.001270	0.043736	0.000639	9.864293	276	3.95	86%	0.104
Jiamanhaba 23	92.71	304.48	1987.76	0.071074	0.001739	0.042786	0.000523	6.661006	270	3.24	72%	0.153
Jiamanhaba 24	123.06	152.18	2937.72	0.051092	0.001126	0.041639	0.000539	19.728021	263	3.34	99%	0.052
Jiamanhaba 25	132.48	323.06	3776.90	0.089738	0.001970	0.030039	0.000360	11.893359	191	2.25	48%	0.086
Jiamanhaba 26	129.15	110.43	3129.59	0.050805	0.001134	0.040989	0.000522	29.070767	259	3.23	99%	0.035
Jiamanhaba 27	7.64	106.64	77.86	0.053176	0.003443	0.067581	0.001249	0.750263	422	7.55	96%	1.370
Jiamanhaba 28	116.67	146.08	2760.23	0.056010	0.001246	0.041123	0.000469	19.506242	260	2.91	92%	0.053
Jiamanhaba 29	77.23	120.85	1868.87	0.055988	0.001390	0.040142	0.000451	15.833978	254	2.80	92%	0.065
Jiamanhaba 30	283.45	271.94	6619.34	0.060757	0.001734	0.041453	0.000509	24.754284	262	3.15	84%	0.041
Amulagong 01	15.83	0.83	1497.69	0.054734	0.001571	0.058838	0.001381	2911.375377	369	8.41	98%	0.001
Amulagong 02	95.80	4.07	1534.46	0.056518	0.001645	0.058977	0.001903	612.062711	369	11.58	95%	0.003
Amulagong 03	2.74	3.71	2304.46	0.054474	0.001666	0.060976	0.001447	642.321830	382	8.80	99%	0.002
Amulagong 04	0.10	2.99	1777.93	0.053565	0.001941	0.061402	0.001472	628.623270	384	8.94	99%	0.002
Amulagong 05	0.01	6.17	2559.35	0.054624	0.001675	0.060100	0.001405	424.756847	376	8.55	98%	0.002
Amulagong 06	416.81	7.33	2855.01	0.056667	0.001788	0.058720	0.001484	418.729516	368	9.04	95%	0.003
Amulagong 07	1.41	6.32	2306.08	0.055047	0.001822	0.058851	0.001395	375.576182	369	8.50	97%	0.003
Amulagong 08	27.34	1.16	1159.36	0.055431	0.002187	0.059972	0.001409	1067.137138	375	8.57	97%	0.001
Amulagong 09	20.29	4.43	2782.25	0.053819	0.001593	0.060174	0.001506	644.785354	377	9.16	99%	0.002
Amulagong 10	6.44	1.72	1317.29	0.054472	0.002047	0.059648	0.001419	807.019061	373	8.64	98%	0.001
Amulagong 11	1.44	10.46	3837.11	0.056838	0.001774	0.060027	0.001546	374.449433	376	9.40	95%	0.003
Amulagong 12	14.86	4.51	1374.01	0.057896	0.001842	0.060309	0.001492	315.800502	378	9.07	94%	0.003

Table 2. *Cont.*

Sample	Pb	Th	U	$^{207}Pb/^{206}Pb$		$^{206}Pb/^{238}U$		$^{238}U/^{232}Th$	$^{206}Pb/^{238}U$		Concordance	Th/U
	ppm	ppm	ppm	Ratio	1 Sigma	Ratio	1 Sigma	Ratio	Age (Ma)	1 Sigma		
Amulagong 13	0.47	1.32	1338.74	0.055119	0.001875	0.060582	0.001422	1082.378851	379	8.65	98%	0.001
Amulagong 14	0.31	3.31	1120.51	0.056670	0.001687	0.068982	0.001576	352.629848	430	9.51	97%	0.003
Amulagong 15	11.04	4.11	2089.54	0.058551	0.002129	0.062841	0.001495	543.342589	393	9.07	93%	0.002
Tiemulete 01	740.00	696.37	3135.78	0.425251	0.013040	0.095003	0.001494	4.974462	585	8.80	−7%	0.222
Tiemulete 02	670.93	319.98	2773.61	0.465163	0.011346	0.094877	0.001727	8.799213	584	10.17	−10%	0.115
Tiemulete 03	488.70	100.55	4255.11	0.220619	0.008916	0.069567	0.000926	50.724626	434	5.59	9%	0.024
Tiemulete 04	127.64	21.48	2195.46	0.059284	0.001709	0.057870	0.000822	102.790913	363	5.01	91%	0.010
Tiemulete 05	205.14	37.64	3137.53	0.079958	0.004096	0.059860	0.000930	86.099086	375	5.66	67%	0.012
Tiemulete 06	197.92	25.33	3346.64	0.060191	0.001824	0.057921	0.000765	131.858292	363	4.67	90%	0.008
Tiemulete 07	386.66	462.48	2493.92	0.315203	0.006811	0.075770	0.001113	5.654171	471	6.67	−4%	0.185
Tiemulete 08	1284.41	572.01	4300.98	0.540468	0.011528	0.102901	0.001842	7.829960	631	10.77	−11%	0.133
Tiemulete 09	730.01	144.22	4273.16	0.346816	0.008355	0.079125	0.001447	32.160684	491	8.65	−7%	0.034
Tiemulete 10	482.21	309.95	3812.63	0.250423	0.006939	0.070590	0.001051	13.259689	440	6.33	3%	0.081
Tiemulete 11	167.87	7.15	1767.59	0.148054	0.005202	0.079313	0.001958	256.452435	492	11.70	33%	0.004
Tiemulete 12	223.69	41.03	4563.76	0.112827	0.003811	0.069254	0.001795	199.341776	432	10.82	46%	0.009
Tiemulete 13	9.32	6.95	2717.30	0.057503	0.001856	0.056426	0.001676	418.718268	354	10.23	93%	0.003
Tiemulete 14	482.54	57.66	3505.16	0.173041	0.005323	0.066851	0.001657	61.916343	417	10.01	20%	0.016
Tiemulete 15	7.29	6.31	2838.11	0.055940	0.001825	0.055738	0.001400	458.074782	350	8.55	95%	0.002
Tiemulete 16	44.49	2.58	1503.83	0.126596	0.005312	0.063587	0.001844	615.414580	397	11.18	36%	0.002
Tiemulete 17	621.47	11.25	2240.30	0.228988	0.007939	0.073218	0.001650	207.634680	456	9.91	8%	0.005
Tiemulete 18	0.03	3.90	4478.65	0.054815	0.001724	0.056220	0.001328	1215.092676	353	8.11	97%	0.001
Tiemulete 19	669.41	51.03	2395.59	0.219201	0.012017	0.076159	0.002587	56.493580	473	15.50	10%	0.021
Tiemulete 20	92.97	15.21	4232.11	0.111963	0.004121	0.062123	0.001507	295.115984	389	9.15	44%	0.004

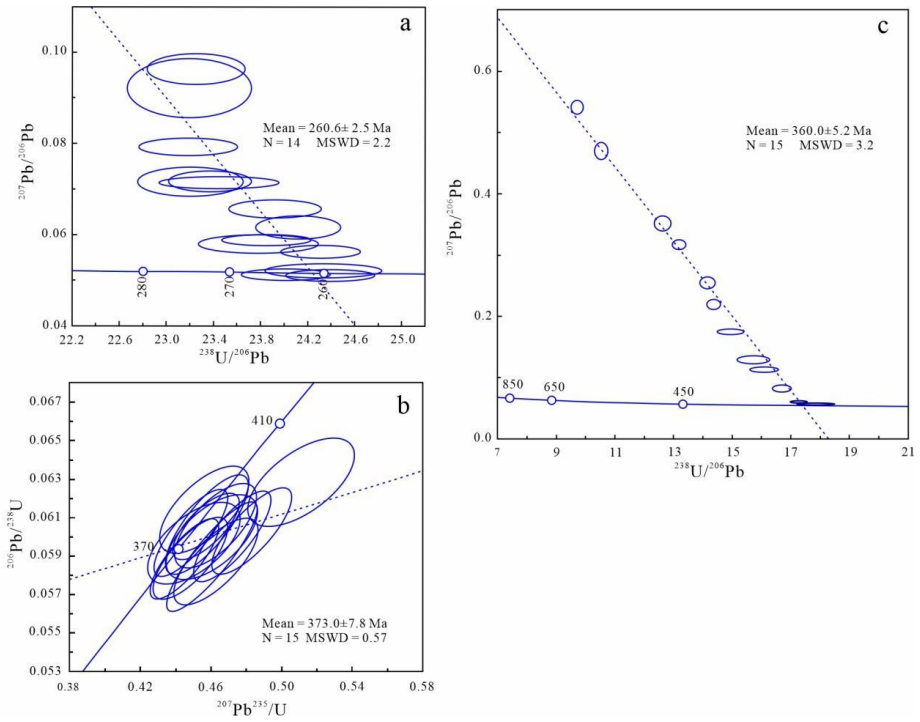

Figure 4. U–Pb concordia diagrams of the Jiamanhaba, Amulagong and Tiemulete pegmatites. (**a**) U–Pb concordia diagrams of Jiamanhaba pegmatite; (**b**) U–Pb concordia diagrams of Amulagong pegmatite; (**c**) U–Pb concordia diagrams of Tiemulete pegmatite.

4.1.2. The Amulagong Pegmatite

Regarding this pegmatite, approximately 60 zircon grains measuring 50–150 μm were separated, and 15 were analysed. Data for a representative subset of the zircons that were analysed are displayed in Figure 3b. The analysed zircons are equiaxial, and these produced comparable aspect ratios of approximately 1:1. These zircons also yielded dark to almost black CL images (Figure 3b), and many crystals exhibited weak magmatic oscillatory annular zones.

Among the 15 zircons that were analysed for U-Pb isotopes, the concentrations of Th and U for the samples range from 0.83 to 10.46 and 1120.51 to 3837.11 ppm, respectively, and these produced Th/U ratios that vary from 0.001 to 0.003, whereas the $^{206}Pb/^{238}U$ages range from 368 to 430 Ma (Table 2). One yielded an age of 430 Ma, and this was considered a xenocryst because the associated age was evidently distinct from those obtained for other samples. Data for the other 14 samples produced a weighted average age of 373.0 ± 7.8 Ma, and this likely represents the age of emplacement of the Amulagong pegmatite (Figure 4b).

4.1.3. Tiemulete Pegmatite

Approximately 60 zircon grains measuring 100–200 μm were separated from samples of this pegmatite, and 20 were analysed. Figure 3c shows data for a representative subset of the analysed zircons. The zircons were short and columnar, and they exhibited aspect ratios that vary from 2:3 to 3:4. These zircons also displayed dark to almost black CL images (Figure 3c), and several crystals were characterised by weak magmatic oscillatory annular zones. The concentrations of Th and U for the zircons analysed range from 2.58 to 696.37 and 1503.83 to 4563.76 ppm, respectively, and these produced Th/U ratios that range from 0.001 to 0.222, whereas the $^{206}Pb/^{238}U$ ages vary from 350 Ma to 631 Ma (Table 2).

Five of the 20 samples that were analysed yielded $^{206}Pb/^{238}U$ ages that ranged from 341 to 585 Ma, and these highlight an obvious deviation from the concordant line. These samples are likely xenocrysts because of their high Th/U ratios of 0.005 to 0.1. The other 15 samples produced a weighted average age of 360 ± 5.2 Ma, and this probably represents the age of emplacement of the Tiemulete pegmatite (Figure 4c).

4.2. Zircon Hf Isotope Compositions

4.2.1. Jiamanhaba Pegmatite

Ten zircon grains from the Jiamanhaba pegmatite were analysed for Lu/Hf isotope compositions, and these samples yielded comparable $^{176}Hf/^{177}Hf$ ratios that vary from 0.2826946 to 0.2827535. The εHf(t) values that were obtained based on the U-Pb age data range from 2.87 to 4.94, whereas the T_{DM2} ages vary from 969 to 1100 Ma (Table 3).

Table 3. Hf isotopic compositions of the Jiamanhaba pegmatite, the Amulagong pegmatite, and the Tiemulete pegmatite, determined by LA-MC-ICPMS.

Sample	$^{176}Yb/^{177}Hf$	1 Sigma	$^{176}Lu/^{177}Hf$	1 Sigma	$^{176}Hf/^{177}Hf$	1 Sigma	Age	εHf(t)	1 Sigma	TDM1	TDM2
Jiamanhaba 01	0.021535	0.000140	0.000693	0.0000032	0.2826946	0.00001	261	2.87	0.4	783	1100
Jiamanhaba 02	0.032983	0.000180	0.001146	0.0000052	0.2827239	0.0000085	261	3.83	0.3	751	1039
Jiamanhaba 03	0.029732	0.000180	0.000808	0.0000039	0.282741	0.0000099	261	4.49	0.4	720	997
Jiamanhaba 04	0.024594	0.000250	0.000634	0.0000051	0.2827507	0.0000083	261	4.87	0.3	703	974
Jiamanhaba 05	0.027514	0.000240	0.000781	0.000005	0.2827535	0.0000087	261	4.94	0.3	702	969
Jiamanhaba 06	0.072113	0.000320	0.002193	0.0000079	0.2827071	0.0000073	261	3.05	0.3	797	1089
Jiamanhaba 07	0.021297	0.000210	0.000629	0.0000057	0.2827268	0.000009	261	4.02	0.3	737	1027
Jiamanhaba 08	0.039408	0.000063	0.001061	0.0000019	0.2827475	0.0000084	261	4.68	0.3	716	985
Jiamanhaba 09	0.040564	0.000210	0.001077	0.0000044	0.2827298	0.000008	261	4.05	0.3	741	1025
Jiamanhaba 10	0.024028	0.000110	0.000704	0.0000033	0.2827298	0.0000078	261	4.11	0.3	734	1021
Amulagong 01	0.003888	0.000012	0.000093	0.00000024	0.2827454	0.000011	373	7.25	0.4	701	909
Amulagong 02	0.001193	0.000004	0.000031	0.00000011	0.28272	0.0000092	373	6.36	0.3	735	965

Table 3. *Cont.*

Sample	$^{176}Yb/^{177}Hf$	1 Sigma	$^{176}Lu/^{177}Hf$	1 Sigma	$^{176}Hf/^{177}Hf$	1 Sigma	Age	εHf(t)	1 Sigma	TDM1	TDM2
Amulagong 03	0.003669	0.000032	0.000088	0.00000092	0.2827115	0.0000087	373	6.05	0.3	748	985
Amulagong 04	0.001810	0.000005	0.000046	0.00000012	0.2827105	0.0000092	373	6.02	0.3	748	987
Amulagong 05	0.003921	0.000045	0.000103	0.0000012	0.2827069	0.00001	373	5.88	0.4	754	996
Amulagong 06	0.007036	0.000083	0.000170	0.000002	0.2827398	0.000035	373	7.03	1.2	710	923
Amulagong 07	0.004397	0.000024	0.000103	0.00000066	0.2827108	0.0000088	373	6.02	0.3	749	987
Amulagong 08	0.002171	0.000036	0.000052	0.00000087	0.282705	0.0000099	373	5.83	0.4	756	999
Amulagong 09	0.001989	0.000004	0.000046	0.00000017	0.2827266	0.0000092	373	6.59	0.3	726	950
Amulagong 10	0.003800	0.000016	0.000094	0.00000039	0.2827494	0.000015	373	7.39	0.5	695	900
Tiemulete 01	0.031169	0.000310	0.000625	0.0000056	0.2826941	0.0000094	360	5.02	0.3	782	1040
Tiemulete 02	0.028038	0.000100	0.000610	0.0000023	0.2826448	0.0000094	360	3.28	0.3	851	1151
Tiemulete 03	0.028071	0.000160	0.000588	0.0000042	0.2826354	0.0000097	360	2.95	0.3	864	1171
Tiemulete 04	0.047595	0.000160	0.001020	0.0000057	0.2826999	0.000011	360	5.13	0.4	782	1033
Tiemulete 05	0.037695	0.000270	0.000772	0.0000059	0.2826919	0.0000084	360	4.90	0.3	789	1048
Tiemulete 06	0.026417	0.000160	0.000580	0.0000028	0.2827263	0.0000085	360	6.17	0.3	737	967
Tiemulete 07	0.033801	0.000320	0.000745	0.0000065	0.2827218	0.0000096	360	5.97	0.3	746	980
Tiemulete 08	0.069240	0.000460	0.001552	0.000013	0.2827049	0.0000079	360	5.18	0.3	787	1030
Tiemulete 09	0.026999	0.000910	0.000668	0.000018	0.2827115	0.000014	360	5.62	0.5	759	1002
Tiemulete 10	0.009072	0.000210	0.000191	0.000005	0.2826961	0.000013	360	5.19	0.5	771	1029

4.2.2. Amulagong Pegmatite

Seventeen zircon grains from the Amulagong pegmatite that were analysed for Lu/Hf isotope compositions also produced comparable $^{176}Hf/^{177}Hf$ ratios of 0.282705 to 0.2827494. The εHf(t) values that were obtained based on the U-Pb data range from 5.83 to 7.39, whereas the T_{DM2} ages vary from 900 to 999 Ma (Table 3).

4.2.3. Tiemulete Pegmatite

Regarding the Tiemulete pegmatite, 10 zircon grains that were separated and analysed for Lu/Hf isotope compositions produced uniform $^{176}Hf/^{177}Hf$ ratios of 0.2826354–0.2827263. The εHf(t) values that were obtained based on the U-Pb data range from 2.95 to 6.17, whereas the T_{DM2} ages vary from 967 to 1171 Ma (Table 3).

4.3. Zircon O Isotopic Compositions

Ten zircons samples that were separated from each of the of the Jiamanhaba, Amulagong and Tiemulete pegmatites were analysed for O isotope compositions and the data are presented in Table 4. The $\delta^{18}O$ data for the Jiamanhaba, Amulagong and Tiemulete samples correspondingly vary from 6.05 to 7.32 ‰ (mean = 6.73‰), 9.55 to 14.27‰ (mean = 12.00‰), and 11.47 to 15.86‰ (mean = 12.61‰).

Table 4. O isotope compositions of Jiamanhaba, Amulagong and Tiemulete pegmatites, determined by sims.

Sample	$^{18}O/^{16}O$	SE (%)	$\delta^{18}O_{correct}$	2SE (‰)
Jiamanhaba 01	0.0020188	0.015	6.77	0.31
Jiamanhaba 02	0.0020193	0.012	7.02	0.23
Jiamanhaba 03	0.0020174	0.008	6.09	0.15
Jiamanhaba 04	0.0020199	0.012	7.32	0.24
Jiamanhaba 05	0.0020173	0.019	6.05	0.38
Jiamanhaba 06	0.0020196	0.014	7.16	0.28
Jiamanhaba 07	0.0020181	0.016	6.42	0.31

Table 4. *Cont.*

Sample	$^{18}O/^{16}O$	SE (%)	$\delta^{18}O_{correct}$	2SE (‰)
Jiamanhaba 08	0.0020186	0.014	6.68	0.29
Jiamanhaba 09	0.0020183	0.016	6.51	0.31
Jiamanhaba 10	0.0020198	0.015	7.29	0.3
Amulagong 01	0.0020298	0.017	12.24	0.33
Amulagong 02	0.002027	0.016	10.89	0.32
Amulagong 03	0.0020324	0.014	13.58	0.29
Amulagong 04	0.0020257	0.016	10.22	0.32
Amulagong 05	0.0020317	0.013	13.23	0.27
Amulagong 06	0.0020279	0.018	11.31	0.37
Amulagong 07	0.0020338	0.014	14.27	0.27
Amulagong 08	0.0020331	0.015	13.9	0.31
Amulagong 09	0.0020268	0.014	10.79	0.29
Amulagong 10	0.0020243	0.016	9.55	0.33
Tiemulete 01	0.0020296	0.023	12.15	0.46
Tiemulete 02	0.0020286	0.016	11.66	0.32
Tiemulete 03	0.0020317	0.022	13.21	0.43
Tiemulete 04	0.0020351	0.015	14.92	0.29
Tiemulete 05	0.0020283	0.012	11.54	0.24
Tiemulete 06	0.002029	0.018	11.85	0.37
Tiemulete 07	0.0020282	0.016	11.47	0.32
Tiemulete 08	0.002037	0.018	15.86	0.36
Tiemulete 09	0.0020288	0.018	11.79	0.35
Tiemulete 10	0.0020286	0.019	11.69	0.37

5. Discussion

5.1. Zircon U-Pb Geochronology

The U-Pb data for samples that were used to calculate Concordia ages are presented in Table 2. However, because data for the main zircon populations from the Jiamanhaba and Tiemulete pegmatites failed to provide corresponding concordant ages, the lower intersection age that was obtained using a T-W diagram was considered the age of emplacement of the associated magma. According to zircon U-Pb dating data, the Jiamanhaba pegmatites were formed in the Early Permian, whereas the other two pegmatites were emplaced in the Late Devonian. Analysis data produced wide Th/U ratios of 0.04 to 1.37 and from 0.001 to 0.222 for samples from the Jiamanhaba and Tiemulete pegmatites, respectively. According to the values of Th/U, several zircons that were obtained from the Jiamanhaba and Tiemulete pegmatites are metamictised, but these are of a magmatic origin. Conversely, data generated from zircons that were collected from the Amulagong pegmatite show a high concordance, and thus, the weighted average age of 373.0 ± 7.8 Ma that was produced from these data is considered representative of the age of emplacement. The metamictisation of zircon grains is suggested to decrease radiogenic Pb content. However, Peucat et al. [102] and Davis and Paces [103] suggested that in shallow deposits, because of the low temperature and lack of fluid activity, the loss of radiogenic Pb from metamictised zircons is negligible. Therefore, if a loss of radiogenic Pb occurred in several zircon grains that are used for dating because of metamictisation, the U-Pb ages obtained can deviate from the concordant line. The deduction of effects of metamorphism on the generated data

can thus provide representative ages of emplacement for the pegmatites. According to previous studies on the Chinese Altay, metamict zircon grains can also provide reliable U-Pb age data for the pegmatites [21–23,49,50,104]. Therefore, the Jiamanhaba, Amulagong, and Tiemulete pegmatites are assigned average weighted ages of 260.6 ± 2.5, 373.0 ± 7.8, and 360 ± 5.2, respectively.

Zircon U-Pb data can also be used to evaluate the associated tectonic settings and petrogenesis of these Early Permian and Late Devonian pegmatites. According to a previous study on tectonism in the Chinese Altay, the Permian and Devonian were peak periods of magmatism. In the study area, granites that are coeval with pegmatites are present in outcrops, and these facilitate investigations on the coupling between tectonism and the formation of the pegmatites studied.

5.2. Source Characteristics

Owing to the significantly higher concentration of Hf relative to its radioactive parent Lu, the Hf isotope composition of zircons remains essentially constant after crystallisation. In addition, the closure temperature of 900 °C for the zircon Hf isotope system is similar to that of the zircon U-Pb system. Thus, the Hf isotope composition of zircon can accurately record the compositions of parent magmas of pegmatites [105]. Furthermore, the narrow ranges of εHf(t) values for the samples studied indicate that the associated Hf isotope systems were closed. The εHf(t) ranges of 2.87–4.94, 5.83–7.39, and 2.95–6.17 for the Jiamanhaba, Amulagong, and Tiemulete samples produced corresponding T_{DM2} age ranges of 969–1100, 900–999, and 967–1171 Ma, respectively, and these values fall between the depleted mantle and CHUR evolution lines. These results indicate that the precursor magmas of the three pegmatites originated from heterogeneous sources. The εHf(t) values of Triassic pegmatites including the Keketuohai No.3, Kelumute No. 112, Kaluan and Asikaerte range correspondingly from 1.25 to 2.39, 0.03 to 2.35, 0.65 to 2.50, and −1.50 to 0.77, and these are associated with model ages of 1102–1174, 1112–1225, and 1090–1213 Ma, respectively [49,50]. Overall, the εHf(t) values for the Triassic pegmatites range from −1.50 to +2.50, and the model ages vary from 1090 to 1225 Ma, which highlight low Hf isotope compositions and high model ages. The εHf(t) values for the Xiaokalasu, Dakalasu, Yelaman, and Jiamanhaba pegmatites range from 1.6 to 4.2, 1.6 to 4.3, 2.4 to 3.3, and 2.87 to 4.94, respectively, and the corresponding model ages involve ranges of 997–1293, 989–1064, and 1050–1110 Ma. Relatedly, Permian pegmatites yield εHf(t) values of 1.6–4.94 and two-stage model ages of 989–1293 Ma, whereas Devonian pegmatites produced εHf(t) values of 2.87–7.39 and two-stage model ages that range from 900 to 1171 Ma. Apparently, the εHf(t) values of the Permian and Devonian pegmatites are significantly higher than those of the Triassic pegmatites. The ranges of εHf(t) values for pegmatites that were formed in these three periods reflect differences in the composition of their sources. These results suggest that the magma of the Permian pegmatites involved a higher input of mantle materials relative to that of the Triassic pegmatites. Alternatively, the parent magma of the Permian pegmatites originated from the partial melting of sedimentary or granitic rocks that are associated with high εHf(t) values. Geochemical data on pegmatites in the Chinese Altay from previous studies show that these rocks were derived from the partial melting of Palaeozoic granites and sedimentary/metasedimentary rocks [21,49,50,106]. Therefore, we compiled εHf(t) data for Palaeozoic granites and sedimentary rocks from the Chinese Altay. Data for the Jiamanhaba–Amulagong–Tiemulete pegmatites fall within the ranges of 17 to 9.8 and 17 to 26 that were obtained for the Palaeozoic granites/gneiss and sedimentary rocks, respectively (Figure 5). These results demonstrate that excluding the mixing of magma, the remelting of pre-existing Palaeozoic granites or sedimentary rocks was adequate to generate the initial magma from which the studied pegmatites were formed. However, the origin of the Jiamanhaba–Amulagong–Tiemulete pegmatites cannot be definitively demonstrated in the present study.

Zircon is a very stable mineral, and the diffusion rate of its oxygen isotope is low; thus, its initial oxygen isotope composition is preserved even after advanced metamor-

phism [107–110]. Therefore, the oxygen isotope composition of zircon can be used as a tracer of sources of ore-forming materials [110–115]. The zircon O isotope values of the Jiamanhaba–Amulagong–Tiemulete pegmatites range from 6.05 to 15.86 ‰ (Table 4, Figure 6), which are higher than those of mantle-derived zircons (5.3 ± 0.3‰). These results indicate that mantle or juvenile materials were involved in the initial magmas from which the Jiamanhaba–Amulagong–Tiemulete pegmatites were formed. Among major rock-forming minerals in these pegmatites, quartz and feldspar exhibit oxygen isotope enrichments. Pegmatites formed through the partial melting of granites should involve quartz and feldspar that show oxygen isotope enrichment relative to the granites [116,117]. According to data shown in Figure 6, the O isotope values of Palaeozoic granites are clearly higher than those of the Jiamanhaba pegmatites and comparable to those of the Amulagong and Tiemulete pegmatites, which demonstrate that these pegmatites were not derived from the partial melting of Palaeozoic granites. According to data that are displayed in Figure 5, the Habahe Group and Kulumuti Formation are part of Unit 2 (Central Altay Terrane). The dating data show that ages of samples from the Habahe Group mostly range from Cambrian to Ordovician, whereas for the Habahe/Kulumuti Formation, these vary from Neoproterozoic to Silurian [35,37,38,118,119]. Unit 3 (Qiongkuer Terrance) comprises the Early Devonian Kangbutiebao and Middle Devonian Altay formations as well as the Cambrian–Ordovician Habahe Group [35,38,84,120–130]. Therefore, the Permian Jiamanhaba pegmatite was most likely derived from the partial melting of sedimentary/metasedimentary rocks of the Kangbutiebao Formation in the northwest of the Qiongkuer Terrance, and minor mantle-derived or juvenile materials were added to the original magma. In contrast, the Devonian Amulagong and Tiemulete pegmatites were probably derived from the partial melting of sedimentary/metasedimentary rocks of the Habahe/Kulumuti Formation in the southeast of the Qiongkuer Terrance, and the original magmas were contaminated by higher amounts of mantle-derived or juvenile materials than that of the Permian pegmatites.

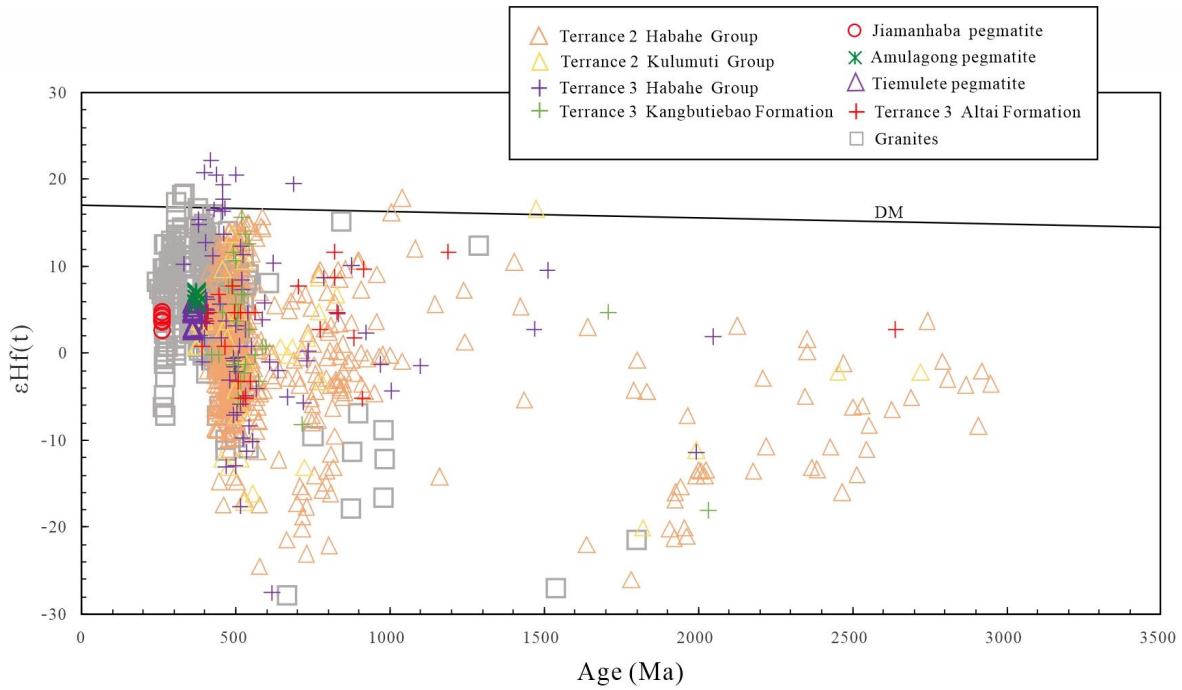

Figure 5. The age vs. εHf(t) diagrams of the Jiamanhaba, Amulagong and Tiemulete pegmatites compared with Paleozoic granites and sedimentary rocks in the Chinese Altay. (The data are from Zhang et al. [21]; Long et al. [35,37]; Sun et al. [38,40]; Lv et al. [50]; Cai et al. [62]; Zhang et al. [73]; Tong et al. [77]; Liu et al. [78]; Yu et al. [85]; Zhao et al. [131]; He et al. [132]; Shen et al. [133]; and Zhang et al. [134]).

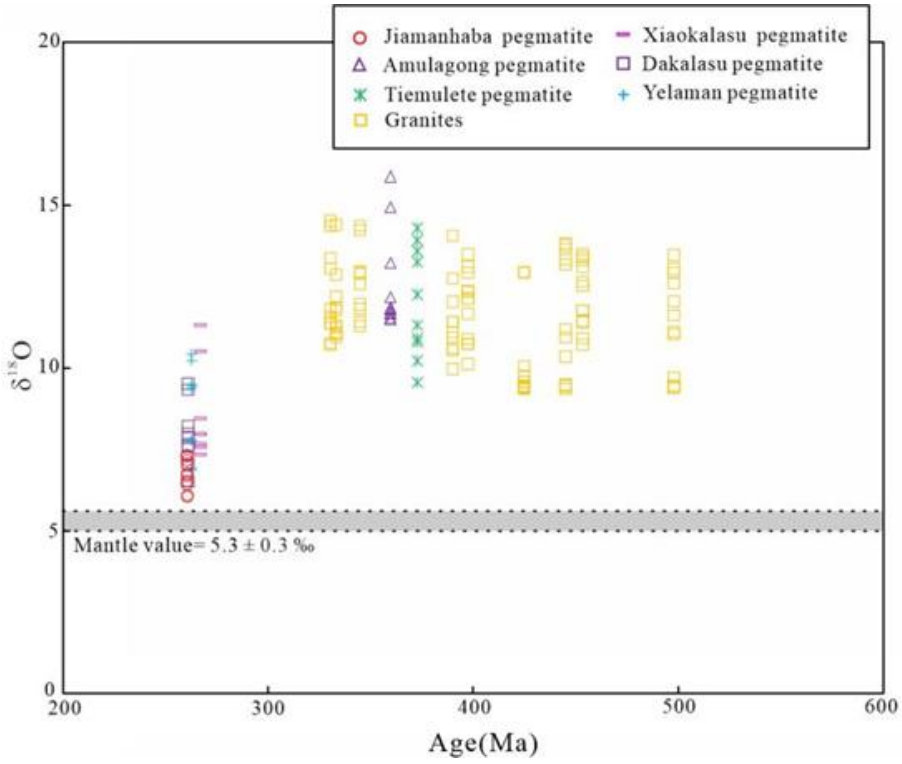

Figure 6. The age vs. δ18O diagrams of the Jiamanhaba, Amulagong and Tiemulete pegmatites, compared with Paleozoic granites in the Chinese Altay. (The data are from Wang et al. [64]; Kong et al. [135]; Zhang et al. [136]).

5.3. Petrogenesis

Pegmatites are petrogenetically distinguished based on their relationships to granites because these are considered late evolution segregation and crystallisation products of granitic magmas. An example is the Li-rich pegmatite in the Songpan–Ganzi Orogenic Belt [137–139]. However, based on geochemical and field studies, an anatexis model was advanced recently for the petrogenesis of pegmatites in the Chinese Altay. Lv et al. [22], for example, suggested that the Baicheng pegmatites originated from the anatexis of metasedimentary rocks in the Qinghe area. In addition, Zhang et al. [21] reported that several Triassic pegmatites originated from partial melting of the Halong granite and sedimentary rocks of the Kulumuti Group. According to previous studies and zircon Hf-O isotope compositions of the Jiamanhaba–Amulagong–Tiemulete pegmatites, it is likely that the pegmatites studied were derived from the partial melting of mature sedimentary rocks, and the original melts were contaminated with mantle-derived or juvenile materials. The differences in $\delta^{18}O$ values between these pegmatites and the Palaeozoic granites indicate the lack of a direct genetic relationship between the former and the latter. Based on the discrepancy of $\delta^{18}O$ value between these pegmatites and Paleozoic granites, we conclude that the pegmatites do not have the direct relationship with Paleozoic granites. This is because the earth crust's average content of beryllium ranges from 2.4 to 4 ppm [140], which is far lower than the beryl saturated crystallisation threshold value of higher than 35 ppm [141,142]. Even if the sedimentary rocks were partially melted in small proportion, it is far from reaching the threshold value of beryl saturated crystallisation. In addition, the Jiamanhaba–Amulagong–Tiemulete pegmatites have a low fraction degree, which also cannot enrich the beryllium content to reach the threshold value of beryl saturated crystallisation. According to the zircon U-Pb dating data, the Jiamanhaba pegmatite was formed in the early Permian, and the others (Amulagong and Tiemulete) were formed in the late Devonian, which show the strong crust–mantle interaction in the two periods. In addition, the available data show two important peaks in Devonian

(ca. 420~380 Ma) and Permian (ca. 290~250 Ma), which counterpart to the Amulagong pegmatite (ca. 373 Ma), Tiemulete pegmatite (ca. 360 Ma) and Jiamanhaba (ca. 261 Ma) pegmatite [40,48,72,77,79,82,88,143–147]. According to classification diagrams (Figure 7), the Permian granites are dominantly I- and S-types, whereas the Devonian granites are mostly the A-type. The A-type granite is commonly associated with anorogenic or post-orogenic settings. Plutons of the Permian granites are approximately elliptical and are restricted by fault zones. Based on geochemical characteristics that were reported in previous studies, the Permian granites were formed in a post-orogenic setting [77,78,87–89,132,134,148–150]. In addition, εHf(t) values of the Permian pegmatites are positive, whereas the coeval granites show both positive and negative values, and these data highlight mantle–crust interactions during the Permian in the Chinese Altay. Discriminant diagrams, including the Nb vs. Y and Rb vs. Y + Nb [151], show almost all Devonian granite samples in the VAG or VAG-SYN-COLG region (Figure 8). These results suggest that the granites are associated with the volcanic arc setting. This is consistent with the previous studies, which show that these Devonian granites were attributed a subduction setting [38,61,62,73,79,85,152]. The positive εHf(t) values for the Middle Devonian to Late Carboniferous granites shown in Figure 9 reveal that mantle-derived magmas associated with the slab window were added to initial magmas of the granites and pegmatites in the Devonian. The late evolution of a granitic magma that was rich in incompatible elements and volatiles elevated the rare metal contents of the pegmatites, which was crucial for the formation of deposits. Mantle-derived magma underplating of the lower crust provided heat and materials, which caused the partial melting of mature sedimentary rocks. These felsic magmas then moved upward and formed pegmatites after crystallisation. The incompatible elements and volatiles associated with coeval granites promote mobility and low solidus temperatures during the late evolution of such magmas. These components can migrate over long distances to elevate the rare metal contents of other fluids, which subsequently form ores [153].

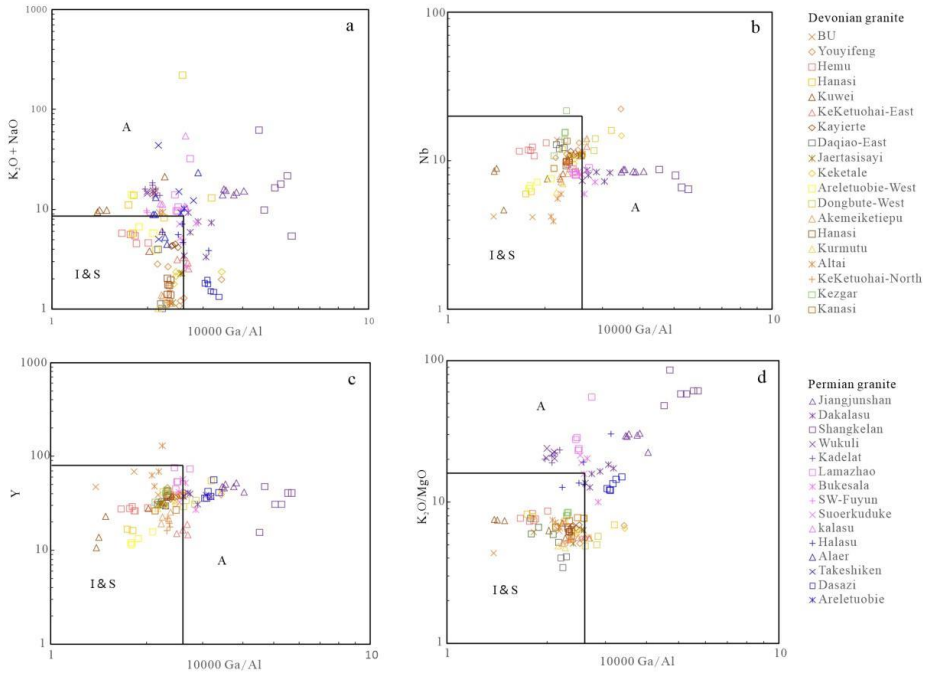

Figure 7. Chemical classification diagrams: (**a**) $K_2O + Na_2O$ versus 10000 Ga/Al; (**b**) Nb versus 10000 Ga/Al; (**c**) Y versus 10000 Ga/Al; and (**d**) K_2O/MgO versus 10000 Ga/Al (The data are from Sun et al. [38]; Cai et al. [61]; Zhang et al. [73]; Tong et al. [77]; Liu et al. [78]; Tong et al. [79]; Yu et al. [85]; Wang et al. [87]; Zhou et al. [88]; Gao et al. [89]; He et al. [132]; Zhang et al. [134]; Tong et al. [148]; Zhang et al. [149]; Lin et al. [150]; and Tong et al. [152]).

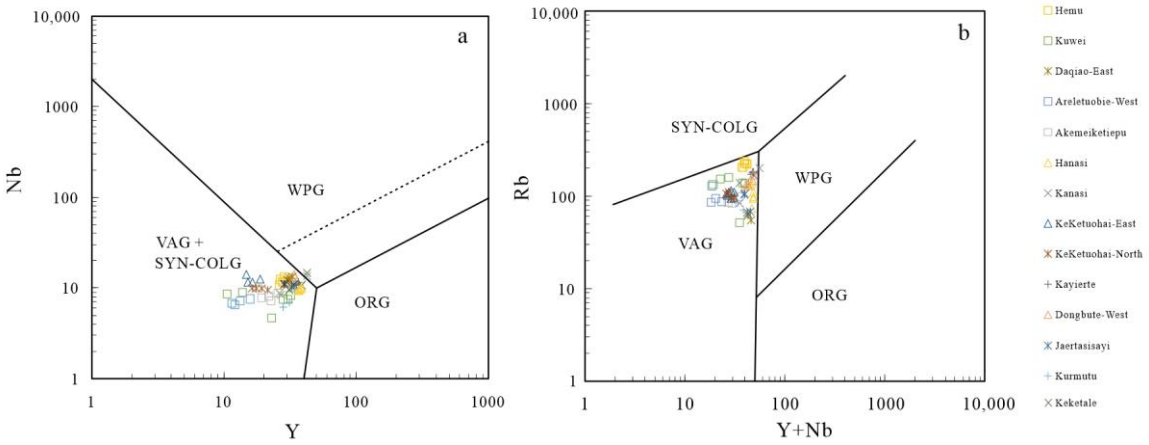

Figure 8. Discriminant diagrams for Devonian granites (**a**) Nb vs. Y diagram, and (**b**) Rb vs. Y + Nb diagram. (The data are collected from Cai et al. [61]; Zhang et al. [73]; Yu et al. [85]; Tong et al. [152]).

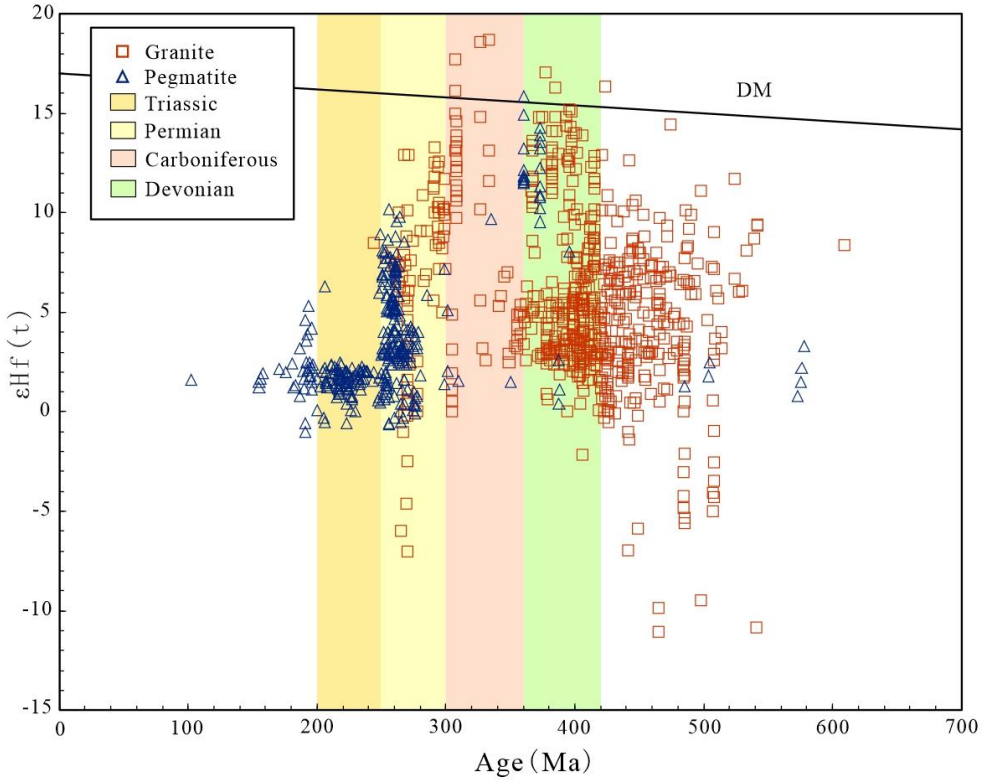

Figure 9. εHf(t) values of granites and pegmatite in four stages in the Chinese Altay (the data are collected from Zhang et al. [21]; Lv et al. [22,23,50]; Sun et al. [38,40]; Ma et al. [49]; Cai et al. [62]; Wang et al. [64]; Zhang et al. [73]; Tong et al. [77]; Liu et al. [78]; Yu et al. [85]; Zhao et al. [131]; He et al. [132]; Shen et al. [133]; and Zhang et al. [134]).

In previous studies, a clear genetic relationship between granites and pegmatites in the Chinese Altay was not established. The genetic relationship between the Alar granite and Keketuohai No. 3 pegmatite, for example, remains a debate, whereas the Jideke and Halong granites have been disproved as parent granites of the Kelumute No. 112 pegmatite and Kaluan–Azubai–Jiamukai pegmatites, respectively. Lv et al. [22,23] therefore proposed an anatexis model for the genesis of these pegmatites. Therefore, even though pegmatites in the Chinese Altay are associated with granitic magmas, they exhibit no direct genetic relationship to coeval granites.

5.4. Implications for Magmatism in the Chinese Altay

The evolution of the Central Asian Orogenic Belt (CAOB) from the Precambrian to Late Palaeozoic remains controversial. According to previous studies, in the Early Palaeozoic, the tectonic setting in this belt was an island arc [31,154] or a passive continental margin [155] or a Precambrian microcontinent [156]. However, based on zircon dating data of granites [35,37,38,40] and petrological and geochemical data for gneissic rocks [38], the CAOB was partitioned into different tectonic units, including the active continental margin, accretionary wedge complex, fore-arc and back-arc basins, and island arcs [33,38, 61,62,72,157]. According to the Wilson Cycle of plate movements, the contraction of an ocean basin begins with subduction of the oceanic crust. In the CAOB, subduction and accretionary orogeny have been experienced since the Neoproterozoic. The Late Palaeozoic collision of the Siberian and Kazakh plates marked the closure of the Irtysh–Zaisan Ocean. Owing to the closure of the ocean basin, the Irtysh Suture Zone then formed through a land-to-land collision, and subsequently, the CAOB was characterised as a post-collision extensional tectonic environment. However, the time of closure of the Irtysh–Zaisan Ocean remains under debate. According to some studies, this occurred during the Early–Middle Devonian [80,158], whereas other studies suggest that this occurred during the Late Devonian–Early Carboniferous [159–161], and closure in the Permian was advanced in others [162–165].

According to the zircon U-Pb dating data for pegmatites in the Chinese Altay, pegmatites in the Qinghe ore deposits area, such as the Amulagong and Tiemulete, were formed during the Devonian [23]. Others including the Xiaokalasu, Dakalasu, Yelaman, Jiamanhaba, Keketuohai No. 3 pegmatite, Kelumute No. 112, Kaluan and Asikaerte are of Permian and Triassic ages [21,44–51]. Previous studies have demonstrated that pegmatite formation commonly occurs in a post-collisional or another extensional setting [3,5,166–170]. Therefore, published geochronological and Hf-O isotopic data for felsic igneous rocks in the Chinese Altay were also examined (Figures 6 and 9). Starting from the Neoproterozoic, the continuous subduction of the oceanic crust created frequent magmatic activities, and these attained a climax at ca. 400 Ma. A significant change in the Hf isotope composition occurred at ca. 400 Ma because before this time, εHf(t) values of zircons were both positive and negative, whereas after this time, all data from zircons analysed are positive. This implies that compositions of initial magmas significantly changed within a short period because of the input of juvenile or depleted mantle materials [33,40,62,171,172]. In addition, the high Hf isotope T_{DM2} ages (900–1171 Ma) and high $\delta^{18}O$ values indicate the presence of abundant ancient sedimentary material in source magmas. In fact, previous studies suggest that the upwelling of mantle materials and heat triggered the partial melting of sedimentary rocks in the middle–lower crust to produce initial magmas of the granites and pegmatites (Amulagong and Tiemulete) [23,38,40,62]. Interestingly, Figure 9 shows obvious changes in εHf(t) and $\delta^{18}O$ values at ca. 300 Ma. In addition, these dramatic changes in εHf(t) and $\delta^{18}O$ values indicate a change in the tectonic setting. According to previous studies, syn-subduction magmatism in the Chinese Altay ended at ca. 313 Ma [72,83]. Furthermore, according to the recent studies, the chronology and Hf isotopic composition of detrital zircons located on the north (The Chinese Altay) and south (West Junggar and East Junggar) sides of the Irtysh suture zone not only reveal that the Irtysh suture zone is the tectonic boundary between the Chinese Altai and East Junggar but also that the Irtysh–Zaisan Ocean is closed at 323 Ma [173–175]. Furthermore, Zircon chronology data from structures in different phase of deformation have constrained the timing of deformation, magmatism and metamorphism events of the Irtysh suture [77,86,119,176]. Therefore, the closure of the Irtysh–Zaisan Ocean likely occurred between Late Carboniferous and Early Permian. Starting from Early Permian to Triassic, pegmatites and A-type granites were increasingly formed in Altay, which involved a post-orogenic extensional tectonic setting. The most common magmatic activity that has been reported for a post-collision tectonic setting is delamination of the lithospheric mantle beneath a thickened crust [177–179]. The upwelling of asthenospheric mantle materials can trigger partial melting of the lower crust and, thus,

trigger a largescale magmatism [180–185]. The changes in εHf(t) and $\delta^{18}O$ values in the study area can be attributed to magmatic source differences. The higher T_{DM2} ages, εHf(t), and $\delta^{18}O$ values for Permian relative to Triassic pegmatites are consistent with an older magmatic source for the former.

Therefore, a multi-stage magmatism model is proposed for the study area from the Early Palaeozoic to Mesozoic (Figure 10), and this is summarised subsequently. (1) The Irtysh–Zaisan Ocean started declining in the Neoproterozoic, and this involved subduction of the oceanic crust on both sides of the ocean ridge into the continental crust of Siberia and Kazakhstan, respectively. However, until the slab window was formed, no clear interaction occurred between the crust and lithospheric mantle. (2) Following the formation of the slab window because of the oceanic ridge subduction, abundant materials were upwelled from mantle. The upwelling elevated the temperature field of the lower crust and altered the composition of the original magma. Partial melting of the lower crust and mixing with mantle materials produced initial magmas of the granites and pegmatites that involved positive εHf(t) values. (3) Starting from Late Carboniferous to Early Permian, the CAOB was transformed from a syn-collision orogenic to a post-collision setting. Delamination of the lithosphere promoted the upwelling of mantle materials under the extensional setting [64]. (4) Upon the onset of asthenospheric upwelling, the magmatism probably originated as deep in the crust as near the top of the Moho surface.

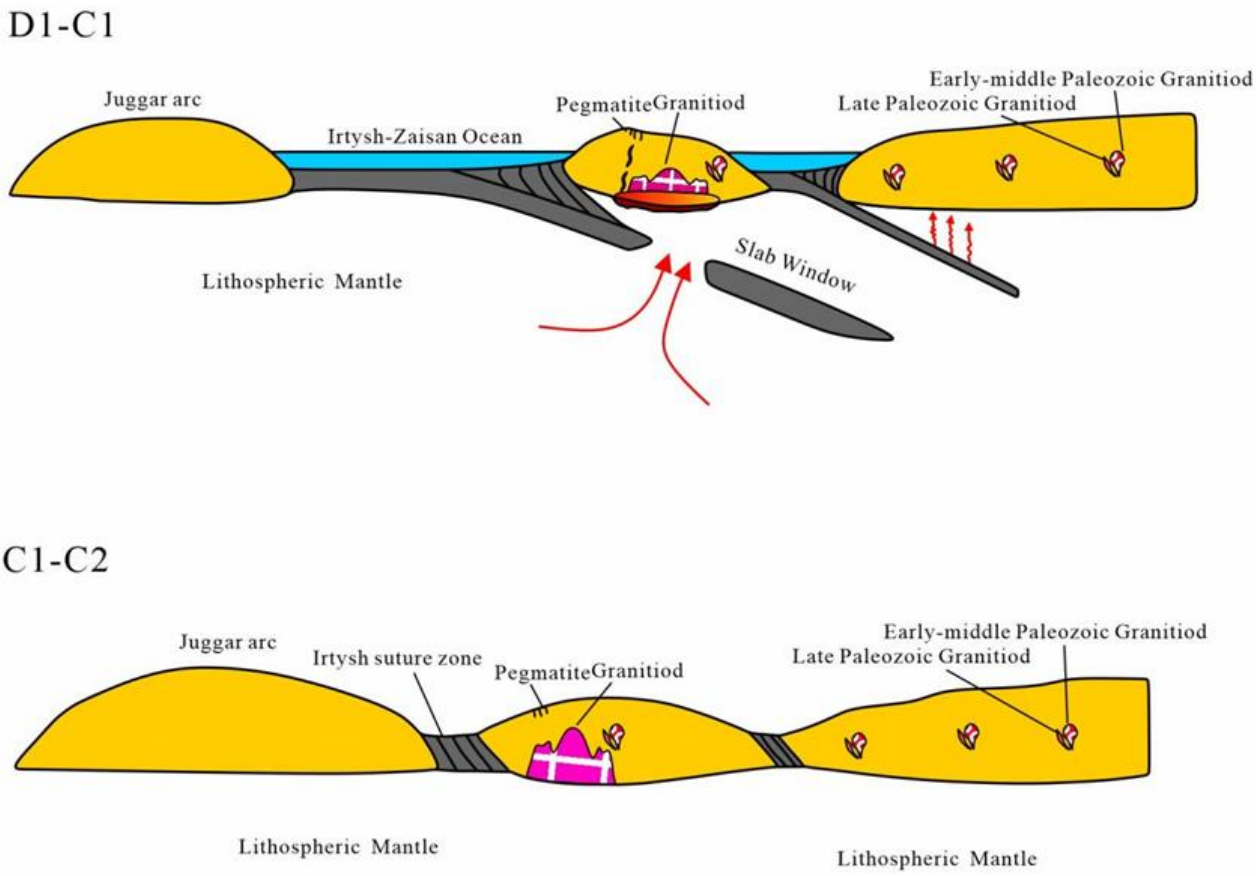

Figure 10. Multi-stage magmatism in the Chinese Altay from Devonian to Early Permian.

6. Conclusions

In the present study, the Jiamanhaba, Amulagong and Tiemulete pegmatites were characterised using zircon U-Pb geochronology and Hf and O isotopes, and the main findings can be summarised as follows:

1. The Jiamanhaba, Amulagong and Tiemulete pegmatites were emplaced correspondingly at approximately 261, 373, and 360 Ma. These results indicated that the Jiaman-

haba pegmatites were of Permian age, whereas those of the Amulagong and Tiemulete were Devonian.

2. The εHf(t) values of 2.87–7.39, two-stage model ages of 900–1171 Ma and $\delta^{18}O$ values of 9.55‰–15.86‰ that were obtained from samples of the Amulagong and Tiemulete pegmatites suggested that these were derived from anatexis of mature sedimentary rocks deep in the crust. In contrast, the Jiamanhaba pegmatite samples produced εHf(t) values of 2.87–4.94 and $\delta^{18}O$ values of 6.05‰–7.32‰, which indicate the addition of minor amounts of mantle/juvenile materials to the original magma.
3. Using a combination of available geochronological and Hf-O isotopic data of felsic igneous, sedimentary, and metamorphic rocks that occur in the Chinese Altay, the formation of the Jiamanhaba pegmatite was assigned to a post-collision tectonic setting, where intensive mantle–crustal interactions occurred in the magma source region. In contrast, the Amulagong and Tiemulete pegmatites were formed in a syn-collision tectonic setting, and juvenile or mantle materials that were produced through the slab window were incorporated in the initial magma.
4. This paper puts forward an independent petrogenesis model of pegmatite in Chinese Altay, that is, the genesis of deep melting, which is different from the previous hypothesis that the pegmatite in Chinese Altay consists of fractionation products of granites during the late fractionation stage and provides reliable evidence for the deep melting of pegmatite. The Hf-O isotopic data of pegmatite and granites and sedimentary rocks in this region reveal the tectonic evolution of the region from Devonian to Permian, and they put forward the closing time of the Irtysh–Zaisan Ocean at about 300 Ma in the Late Carboniferous. The Hf-O isotope data of pegmatite provide a new perspective for revealing the tectonic setting of pegmatite formation, which in turn confines the petrogenesis of pegmatite. The coupling of the two relations provides a reliable guarantee for the study of petrogenesis of pegmatites in different periods in the Chinese Altay.

Author Contributions: Conceptualization, M.W. and X.Z.; methodology, M.W.; software, M.W.; validation, M.W. and X.Z.; formal analysis, M.W.; investigation, M.W.; resources, M.W.; data curation, M.W.; writing—original draft preparation, M.W.; writing—review and editing, M.W.; visualization, M.W.; supervision, X.Z.; project administration, X.Z.; funding acquisition, X.Z. All authors have read and agreed to the published version of the manuscript.

Funding: This research was funded by Regional Science Fund Project of National Natural Science Foundation of China 42062004 And The APC was funded by 42062004.

Data Availability Statement: Data will be made available on request.

Conflicts of Interest: The authors declare no conflict of interest.

References

1. London, D. Pegmatites. *Can. Mineral. Spec. Publ.* **2008**, *10*, 1–347.
2. London, D. Ore-forming processes within granitic pegmatites. *Ore Geol. Rev.* **2018**, *101*, 349–383. [CrossRef]
3. Tkachev, A. Evolution of metallogeny of granitic pegmatites associated with orogens throughout geological time. *Geol. Soc. Lond. Spec. Publ.* **2011**, *350*, 7–23. [CrossRef]
4. McCauley, A.; Bradley, D.C. The global age distribution of granitic pegmatites. *Can. Mineral.* **2014**, *52*, 183–190. [CrossRef]
5. Zagorsky, V.Y.; Vladimirov, A.; Makagon, V.; Kuznetsova, L.; Smirnov, S.; D'yachkov, B.; Annikova, I.Y.; Shokalsky, S.; Uvarov, A. Large fields of spodumene pegmatites in the settings of rifting and post-collisional shear-pull-apart dislocations of continental lithosphere. *Russ. Geol. Geophys.* **2014**, *55*, 237–251. [CrossRef]
6. Ginsburg, A.I.; Timofeyev, I.N.; Feldman, L.G. Principles of Geology of the Granitic Pegmatites. *Nedra Mosc. USSR* **1979**, 296. (In Russian)
7. Černý, P.; Ercit, T.S. The classification of granitic pegmatites revisited. *Can. Mineral.* **2005**, *43*, 2005–2026. [CrossRef]
8. Černý, P. Exploration Strategy and Methods for Pegmatite Deposits of Tantalum. In *Lanthanides, Tantalum and Niobium*; Möller, P., Černý, P., Saupé, F., Eds.; Springer: Berlin/Heidelberg, Germeny, 1989; pp. 274–302.
9. Černý, P. Petrogenesis of granitic pegmatites. In *Granitic Pegmatites in Science and Industry: A Short Course*; Mineralogical Association of Canada: Québec, QC, Canada, 1982; Volume 8, pp. 405–462.
10. Černý, P.; Meintzer, R.E. Fertile granites in the Archean and Proterozoic fields of rare-element pegmatites: Crustal environment, geochemistry and petrogenetic relationships. *Recent Adv. Geol. Granite-Relat. Miner. Depos.* **1988**, *39*, 170–206.

11. Breaks, F.W.; Moore, J.M. The Ghost Lake Batholith, Superior Province of northwestern Ontario; a fertile, S-type, peraluminous granite-rare-element pegmatite system. *Can. Mineral.* **1992**, *30*, 835–875.
12. Černý, P. Fertile granites of Precambrian rare-element pegmatite fields: Is geochemistry controlled by tectonic setting or source lithologies? *Precambrian Res.* **1991**, *51*, 429–468. [CrossRef]
13. Selway, J.B.; Breaks, F.W.; Tindle, A.G. A review of rare-element (Li-Cs-Ta) pegmatite exploration techniques for the Superior Province, Canada, and large worldwide tantalum deposits. *Explor. Min. Geol.* **2005**, *14*, 1–30. [CrossRef]
14. Jahns, R.H.; Burnham, C.W. Experimental studies of pegmatite genesis; l, A model for the derivation and crystallization of granitic pegmatites. *Econ. Geol.* **1969**, *64*, 843–864. [CrossRef]
15. London, D.; Hervig, R.L.; Morgan, G.B. Melt-vapor solubilities and elemental partitioning in peraluminous granite-pegmatite systems: Experimental results with Macusani glass at 200 MPa. *Contrib. Mineral. Petrol.* **1988**, *99*, 360–373. [CrossRef]
16. London, D.; Morgan, V.I.G.B.; Hervig, R.L. Vapor-undersaturated experiments in the system macusanite-H_2O at 200 MPa, and the internal differentiation of granitic pegmatites. *Contrib. Mineral. Petrol.* **1989**, *102*, 1–17. [CrossRef]
17. London, D. The origin of primary textures in granitic pegmatites. *Can. Mineral.* **2009**, *47*, 697–724. [CrossRef]
18. Shearer, C.K.; Papike, J.J.; Jolliff, B.L. Petrogenetic links among granites and pegmatites in the Harney Peak rare-element granite-pegmatite system, Black Hills, South Dakota. *Can. Mineral.* **1992**, *30*, 785–809.
19. Stewart, D.B. Petrogenesis of lithium-rich pegmatites. *Am. Mineral.* **1978**, *63*, 970–980.
20. Henderson, I.H.C.; Ihlen, P.M. Emplacement of polygeneration pegmatites in relation to Sveco-Norwegian contractional tectonics: Examples from southern Norway. *Precambrian Res.* **2004**, *133*, 207–222. [CrossRef]
21. Zhang, X.; Zhang, H.; Ma, Z.-L.; Tang, Y.; Lv, Z.-H.; Zhao, J.-Y.; Liu, Y.-L. A new model for the granite–pegmatite genetic relationships in the Kaluan–Azubai–Qiongkuer pegmatite-related ore fields, the Chinese Altay. *J. Asian Earth Sci.* **2016**, *124*, 139–155. [CrossRef]
22. Lv, Z.-H.; Zhang, H.; Tang, Y. Anatexis origin of rare metal/earth pegmatites: Evidences from the Permian pegmatites in the Chinese Altai. *Lithos* **2021**, *380*, 105865. [CrossRef]
23. Lv, Z.-H.; Zhang, H.; Tang, Y.; Liu, Y.-L.; Zhang, X. Petrogenesis of syn-orogenic rare metal pegmatites in the Chinese Altai: Evidences from geology, mineralogy, zircon U-Pb age and Hf isotope. *Ore Geol. Rev.* **2018**, *95*, 161–181. [CrossRef]
24. Dill, H.G. *The Hagendorf-Pleystein Province: The Center of Pegmatites in an Ensialic Orogen*; Springer: Cham, Switzerland, 2015; Volume 15, pp. 1–465.
25. Dill, H.G. Pegmatites and aplites: Their genetic and applied ore geology. *Ore Geol. Rev.* **2015**, *69*, 417–561. [CrossRef]
26. Melleton, J.; Gloaguen, E.; Frei, D.; Novák, M.; Breiter, K. How are the emplacement of rare-element pegmatites, regional metamorphism and magmatism interrelated in the Moldanubian domain of the Variscan Bohemian Massif, Czech Republic? *Can. Mineral.* **2012**, *50*, 1751–1773. [CrossRef]
27. Müller, A.; Ihlen, P.M.; Snook, B.; Larsen, R.B.; Flem, B.; Bingen, B.; Williamson, B.J. The chemistry of quartz in granitic pegmatites of southern Norway: Petrogenetic and economic implications. *Econ. Geol.* **2015**, *110*, 1737–1757. [CrossRef]
28. Müller, A.; Romer, R.L.; Szuszkiewicz, A.; Ilnicki, S.; Szełęg, E. Can pluton-related and pluton-unrelated granitic pegmatites be distinguished by their chemistry? In Proceedings of the Second Eugene E. Foord Pegmatite Symposium, Denver, CO, USA, 15–19 July 2016; pp. 67–69.
29. Müller, A.; Romer, R.L.; Pedersen, R.B. The Sveconorwegian Pegmatite Province–Thousands of pegmatites without parental granites. *Can. Mineral.* **2017**, *55*, 283–315. [CrossRef]
30. Simmons, W.B.; Falster, A.U. Evidence for an Anatectic Origin of an LCT Type Pegmatite: Mt. Mica, Maine. In Proceedings of the Second Eugene E. Foord Pegmatite Symposium, Golden, CO, USA, 15 July 2016; Volume 103.
31. Sengör, A.M.C.; Natalín, B.A.; Burtman, V.S. Evolution of the Altayd tentonic collage and Paleozoic crustal growth in Eurasia. *Nature* **1993**, *364*, 299–307. [CrossRef]
32. Windley, B.F.; Kröner, A.; Guo, J.; Qu, G.; Li, Y.; Zhang, C. Neoproterozoic to Paleozoic geology of the Altai orogen, NW China: New zircon age data and tectonic evolution. *J. Geol.* **2002**, *110*, 719–737. [CrossRef]
33. Windley, B.F.; Alexeiev, D.; Xiao, W.; Kröner, A.; Badarch, G. Tectonic models for accretion of the Central Asian Orogenic Belt. *J. Geol. Soc.* **2007**, *164*, 31–47. [CrossRef]
34. Xiao, W.; Windley, B.F.; Badarch, G.; Sun, S.; Li, J.; Qin, K.; Wang, Z. Palaeozoic accretionary and convergent tectonics of the southern Altaids: Implications for the growth of Central Asia. *J. Geol. Soc.* **2004**, *161*, 339–342. [CrossRef]
35. Long, X.; Sun, M.; Yuan, C.; Xiao, W.; Lin, S.; Wu, F.; Xia, X.; Cai, K. Detrital zircon age and Hf isotopic studies for metasedimentary rocks from the Chinese Altai: Implications for the Early Paleozoic tectonic evolution of the Central Asian Orogenic Belt. *Tectonics* **2007**, *26*, TC5015. [CrossRef]
36. Long, X.; Sun, M.; Yuan, C.; Xiao, W.; Cai, K. Early Paleozoic sedimentary record of the Chinese Altai: Implications for its tectonic evolution. *Sediment. Geol.* **2008**, *208*, 88–100. [CrossRef]
37. Long, X.; Yuan, C.; Sun, M.; Xiao, W.; Zhao, G.; Wang, Y.; Cai, K.; Xia, X.; Xie, L. Detrital zircon ages and Hf isotopes of the early Paleozoic flysch sequence in the Chinese Altai, NW China: New constrains on depositional age, provenance and tectonic evolution. *Tectonophysics* **2010**, *480*, 213–231. [CrossRef]
38. Sun, M.; Yuan, C.; Xiao, W.; Long, X.; Xia, X.; Zhao, G.; Lin, S.; Wu, F.; Kröner, A. Zircon U–Pb and Hf isotopic study of gneissic rocks from the Chinese Altai: Progressive accretionary history in the early to middle Palaeozoic. *Chem. Geol.* **2008**, *247*, 352–383. [CrossRef]

39. Sun, G.; Li, J.; Yang, T.; Li, Y.; Zhu, Z.; Yang, Z. Zircon SHRIMP U-Pb dating of two linear granite plutons in southern Altay Mountains and its tectonic implications. *Geol. China* **2009**, *36*, 976–987.
40. Sun, M.; Long, X.; Cai, K.; Jiang, Y.; Wang, B.; Yuan, C.; Zhao, G.; Xiao, W.; Wu, F. Early Paleozoic ridge subduction in the Chinese Altai: Insight from the abrupt change in zircon Hf isotopic compositions. *Sci. China Ser. D Earth Sci.* **2009**, *52*, 1345–1358. [CrossRef]
41. Wu, B.Q.; Zou, T.R. The genesis of granitic pegmatites in Xinjiang Altai. *Min. Geol. Xinjiang* **1989**, *1*, 60–70. (In Chinese)
42. Wang, D.H.; Chen, Y.C.; Xu, Z.G. *Metallogenetic Series and Regularity of the Altay Metallogenic Province*; Atomic Energy Press: Beijing, China, 2002; pp. 1–493. (In Chinese)
43. Wang, D.H.; Zou, T.R.; Xu, Z.G.; Yu, J.J. Advance in the study of using pegmatite deposits as the tracer of orogenic process. *Adv. Earth Sci.* **2004**, *19*, 614–620, (In Chinese with English abstract).
44. Zhu, Y.-F.; Zeng, Y.; Gu, L. Geochemistry of the rare metal-bearing pegmatite No. 3 vein and related granites in the Keketuohai region, Altay Mountains, northwest China. *J. Asian Earth Sci.* **2006**, *27*, 61–77. [CrossRef]
45. Wang, T.; Tong, Y.; Jahn, B.-m.; Zou, T.-r.; Wang, Y.-b.; Hong, D.-w.; Han, B.-f. SHRIMP U–Pb Zircon geochronology of the Altai No. 3 Pegmatite, NW China, and its implications for the origin and tectonic setting of the pegmatite. *Ore Geol. Rev.* **2007**, *32*, 325–336. [CrossRef]
46. Chen, J.F. Geochemistry of the Plate Part in Altay No. 3 Pegmatite and Its Formation and Evolution. Master's Thesis, University of Chinese Academy of Sciences, Beijing, China, 2011; pp. 1–86, (In Chinese with English Abstract).
47. Liu, F.; Zhang, Z.-X.; Li, Q.; Zhang, C.; Li, C. New precise timing constraint for the Keketuohai No. 3 pegmatite in Xinjiang, China, and identification of its parental pluton. *Ore Geol. Rev.* **2014**, *56*, 209–219. [CrossRef]
48. Che, X.-D.; Wu, F.-Y.; Wang, R.-C.; Gerdes, A.; Ji, W.-Q.; Zhao, Z.-H.; Yang, J.-H.; Zhu, Z.-Y. In situ U–Pb isotopic dating of columbite–tantalite by LA–ICP–MS. *Ore Geol. Rev.* **2015**, *65*, 979–989. [CrossRef]
49. Ma, Z.; Zhang, H.; Tang, Y.; Lv, Z.; Zhang, X.; Zhao, J. Zircon U-Pb geochronology and Hf isotopes of pegmatites from the Kaluan mining area in the Altay, Xinjiang and their genetic relationship with the Halong granite. *Geochimica* **2015**, *44*, 9–26.
50. Lv, Z.-H.; Zhang, H.; Tang, Y.; Guan, S.-J. Petrogenesis and magmatic–hydrothermal evolution time limitation of Kelumute No. 112 pegmatite in Altay, Northwestern China: Evidence from zircon UPb and Hf isotopes. *Lithos* **2012**, *154*, 374–391. [CrossRef]
51. Ren, B.Q.; Zhang, H.; Tang, Y.; Lv, Z.H. LA-ICPMS U-Pb zircon geochronology of the Altay pegmatites and its geological significance. *Acta Mineral. Sin.* **2011**, *31*, 587–596, (In Chinese with English Abstract).
52. Wang, D.H.; Chen, M.C.; Xu, Z.G. The metallogenic age evidence of metamorphogenic pegmatitic Muscovite deposit in the Altai Caledonian Age and its significance. *Acta Geol. Sin.* **2001**, *3*, 419–425. (In Chinese)
53. Zhou, Q.; Qin, K.; Tang, D.; Tian, Y.; Cao, M.; Wang, C. Formation Age and Evolution Time Span of the Koktokay No. 3 Pegmatite, Altai, NW China: Evidence from U–Pb Zircon and 40Ar–39Ar Muscovite Ages. *Resour. Geol.* **2015**, *65*, 210–231. [CrossRef]
54. Zhou, Q.; Qin, K.; Tang, D.; Wang, C.; Sakyi, P.A. LA-ICP-MS U–Pb zircon, columbite-tantalite and 40Ar–39Ar muscovite age constraints for the rare-element pegmatite dykes in the Altai orogenic belt, NW China. *Geol. Mag.* **2018**, *155*, 707–728. [CrossRef]
55. Qin, K.; Shen, M.; Tang, D.; Guo, Z.; Zhou, Q.; Wang, C.; Guo, X.; Tian, Y.; Ding, J. Types, intrusive and mineralization ages of pegmatite rare-element deposits in Chinese Altay. *Xinjiang Geol.* **2013**, *31* (Suppl. S1), 1–7.
56. Liu, W.-z.; Zhang, H.; Tang, H.-f.; Tang, Y.; Lü, Z.-h. Molybdenite Re-Os dating of the Asikaerte Be-Mo deposit in Xinjiang, China and its genetic implications. *Geochimica* **2015**, *44*, 145–154, (In Chinese with English Abstract).
57. Wang, C.; Qin, K.; Tang, D.; Zhou, Q.; Shen, M.; Guo, Z.; Guo, X. Geochronology and Hf isotope of zircon for the Arskartor Be-Nb-Mo deposit in Altay and its geological implcations. *Atca Petrol. Sin.* **2015**, *31*, 2337–2352, (In Chinese with English Abstract).
58. Zhang, H.; Tang, Y.; Lv, Z.H.; Wen, X.P. Study on metallogenic regularity and prospecting target prediction of rare metals in Halong-Qinghe area, Altai Metallogenic Belt, Xinjiang. *Res. Rep. Xinjiang Nonferrous Met. Group* **2014**, 1–154. (In Chinese)
59. Yang, F.Q.; Geng, X.X.; Wang, R.; Zhang, Z.X.; Guo, X.J. A synthesis of mineralization styles and geodynamic settings of the Paleozoic and Mesozoic metallic ore deposits in the Altay Mountains, NW China. *J. Asian Earth Sci.* **2018**, *159*, 233–258. [CrossRef]
60. Xiao, W.; Windley, B.; Yuan, C.; Sun, M.; Han, C.; Lin, S.; Chen, H.; Yan, Q.; Liu, D.; Qin, K. Paleozoic multiple subduction-accretion processes of the southern Altayds. *Am. J. Sci.* **2009**, *309*, 221–270. [CrossRef]
61. Cai, K.; Sun, M.; Yuan, C.; Zhao, G.; Xiao, W.; Long, X.; Wu, F. Geochronology, petrogenesis and tectonic significance of peraluminous granites from the Chinese Altai, NW China. *Lithos* **2011**, *127*, 261–281. [CrossRef]
62. Cai, K.; Sun, M.; Yuan, C.; Zhao, G.; Xiao, W.; Long, X.; Wu, F. Prolonged magmatism, juvenile nature and tectonic evolution of the Chinese Altai, NW China: Evidence from zircon U–Pb and Hf isotopic study of Paleozoic granitoids. *J. Asian Earth Sci.* **2011**, *42*, 949–968. [CrossRef]
63. Xiao, W.J.; Santosh, M. The western Central Asian Orogenic Belt: A window to accretionary orogenesis and continental growth. *Gondwana Res.* **2014**, *25*, 1429–1444. [CrossRef]
64. Wang, M.-T.; Zhang, H.; Zhang, X.; Tang, Y.; Lv, Z.-H.; Chen, J.-Z.; An, Y. Petrogenetic studies of Permian pegmatites in the Chinese Altay: Implications for a two-stage post-collisional magmatism model. *Geol. J.* **2023**, *58*, 410–427. [CrossRef]
65. Zhou, G.; Zhang, Z.C.; HE, B.; Wang, X.; Li, J.G.; He, Y.K.; Zheng, K.P.; Luo, S.B. SHRIMP zircon U-Pb dating of gneisses in the MayinObo fault belt, northern Xinjiang, and its significance. *Geol. China* **2006**, *33*, 1209–1216.
66. Wang, T.; Hong, D.-w.; Jahn, B.-m.; Tong, Y.; Wang, Y.-b.; Han, B.-f.; Wang, X.-x. Timing, petrogenesis, and setting of Paleozoic synorogenic intrusions from the Altai Mountains, Northwest China: Implications for the tectonic evolution of an accretionary orogen. *J. Geol.* **2006**, *114*, 735–751. [CrossRef]

67. Lv, Z.H.; Zhang, H.; Tang, Y. The study of genetic relationship between Bieyesamasi No. L1 pegmatite Li-Nb-Ta ore deposit and wall rock granite, Xinjiang. *Acta Mineral. Sin.* **2015**, *1*, 323. (In Chinese)
68. Qin, J.H.; Geng, X.X.; Wen, C.Q.; Guo, J.X.; Ren, Y.C. Zircon LA-ICP-MS U-Pb age of intrusion from Xiaotuergen copper deposit in Altay, Xinjiang, and its geological significance. *Miner. Depos.* **2016**, *35*, 18–32, (In Chinese with English Abstract).
69. Yuan, F.; Zhou, T.F.; Yue, S.C. The ages and genetic types of the granites in the Nurtarea, Altai. *Xinjiang Geol.* **2001**, *19*, 292–296, (In Chinese with English Abstract).
70. Wang, T.; Jahn, B.-M.; Kovach, V.P.; Tong, Y.; Hong, D.-W.; Han, B.-F. Nd–Sr isotopic mapping of the Chinese Altai and implications for continental growth in the Central Asian Orogenic Belt. *Lithos* **2009**, *110*, 359–372. [CrossRef]
71. Wang, T.; Tong, Y.; Li, S.; Zhang, J.; Shi, X.; Li, J.; Han, B.-F.; Hong, D. Spatial and temporal variations of granitoids in the Altay orogen and their implications for tectonic setting and crustal growth: Perspectives from Chinese Altay. *Acta Petrol. Mineral.* **2010**, *29*, 595–618.
72. Yuan, C.; Sun, M.; Xiao, W.; Li, X.; Chen, H.; Lin, S.; Xia, X.; Long, X. Accretionary orogenesis of the Chinese Altai: Insights from Paleozoic granitoids. *Chem. Geol.* **2007**, *242*, 22–39. [CrossRef]
73. Zhang, C.; Liu, L.; Santosh, M.; Luo, Q.; Zhang, X. Sediment recycling and crustal growth in the Central Asian Orogenic Belt: Evidence from Sr–Nd–Hf isotopes and trace elements in granitoids of the Chinese Altay. *Gondwana Res.* **2017**, *47*, 142–160. [CrossRef]
74. BGMRX (Bureau of Geology and Mineral Resources of Xinjiang Uygur Autonomous Region) Regional Geology of Xinjiang Uygur Autonomous Region, People's Republic of China, Ministry of Geology and Mineral Resources. Regional Geological Survey of Xinjiang. In *Geological Memoirs, Series, Vol. 1, No. 32*; Geological Publishing House: Beijing, China, 1993; pp. 6–206. (In Chinese)
75. Yang, F.; Mao, J.; Liu, F.; Chai, F.; Guo, Z.; Zhou, G.; Geng, X.; Gao, J. Geochronologyand geochemistry of the granites from the Mengku iron deposit, Altay Mountains, northwest China: Implications for its tectonic setting and metallogenesis. *Aust. J. Earth Sci.* **2010**, *57*, 803–818. [CrossRef]
76. Zheng, J.; Chai, F.; Yang, F. The 401–409 Ma Xiaodonggou granitic intrusion: Implications for understanding the Devonian Tectonics of the Northwest China Altaiorogen. *Int. Geol. Rev.* **2016**, *58*, 540–555. [CrossRef]
77. Tong, Y.; Wang, T.; Jahn, B.-m.; Sun, M.; Hong, D.-W.; Gao, J.-F. Post-accretionary permian granitoids in the Chinese Altai orogen: Geochronology, petrogenesis and tectonic implications. *Am. J. Sci.* **2014**, *314*, 80. [CrossRef]
78. Liu, Y.; Zhang, H.; Tang, Y.; Zhang, X.; Lv, Z.; Zhao, J. Petrogenesis and tectonic setting of the Middle Permian A-type granites in Altay, northwestern China: Evidences from geochronological, geochemical, and Hf isotopic studies. *Geol. J.* **2018**, *53*, 527–546. [CrossRef]
79. Tong, Y.; Wang, T.; Siebel, W.; Hong, D.W.; Sun, M. Recognition of early Carboniferous alkaline granite in the southern Altai orogen: Post-orogenic processesconstrained by U-Pb zircon ages, Nd isotopes, and geochemical data. *Int. J. Earth Sci.* **2012**, *101*, 937–950. [CrossRef]
80. Han, B.-f.; Wang, S.-g.; Jahn, B.-m.; Hong, D.-w.; Kagami, H.; Sun, Y.-l. Depleted-mantle source for the Ulungur River A-type granites from North Xinjiang, China: Geochemistry and Nd–Sr isotopic evidence, and implications for Phanerozoic crustal growth. *Chem. Geol.* **1997**, *138*, 135–159. [CrossRef]
81. Chen, B.; Arakawa, Y. Elemental and Nd-Sr isotopic geochemistry of granitoids from the West Junggar foldbelt (NW China), with implications for Phanerozoic continental growth. *Geochim. Cosmochim. Acta* **2005**, *69*, 1307–1320. [CrossRef]
82. Briggs, S.M.; Yin, A.; Manning, C.E.; Chen, Z.-L.; Wang, X.-F.; Grove, M. Late Paleozoic tectonic history of the Ertix Fault in the Chinese Altai and its implications for the development of the Central Asian Orogenic System. *GSA Bull.* **2007**, *119*, 944–960. [CrossRef]
83. Cai, K.; Sun, M.; Yuan, C.; Xiao, W.; Zhao, G.; Long, X.; Wu, F. Carboniferous mantle-derived felsic intrusion in the Chinese Altai, NW China: Implications for geodynamic change of the accretionary orogenic belt. *Gondwana Res.* **2012**, *22*, 681–698. [CrossRef]
84. Chai, F.; Mao, J.; Dong, L.; Yang, F.; Liu, F.; Geng, X.; Zhang, Z. Geochronology of metarhyolites from the Kangbutiebao Formation in the Kelang basin, Altay Mountains, Xinjiang: Implications for the tectonic evolution and metallogeny. *Gondwana Res.* **2009**, *16*, 189–200. [CrossRef]
85. Yu, Y.; Sun, M.; Long, X.; Li, P.; Zhao, G.; Kröner, A.; Broussolle, A.; Yang, J. Whole-rock Nd–Hf isotopic study of I-type and peraluminous granitic rocks from the Chinese Altai: Constraints on the nature of the lower crust and tectonic setting. *Gondwana Res.* **2017**, *47*, 131–141. [CrossRef]
86. Tong, L.; Xu, Y.-G.; Cawood, P.A.; Zhou, X.; Chen, Y.; Liu, Z. Anticlockwise P-T evolution at ~ 280Ma recorded from ultrahigh-temperature metapelitic granulite in the Chinese Altai orogenic belt, a possible link with the Tarim mantle plume? *J. Asian Earth Sci.* **2014**, *94*, 1–11. [CrossRef]
87. Wang, T. Zircon U-Pb SHRIMP age and origin of post-orogenic Lamazhao granitic pluton from Altai orogen: Its implication for vertical continental growth. *Acta Petrol. Sin.* **2005**, *21*, 640–650.
88. Zhou, G.; Zhang, Z.C.; Luo, S.B.; He, B.; Wang, X.; Yin, L.J.; Zhao, H.; Li, A.H.; He, Y.K. Confirmation of high temperature strongly peraluminous Mayin' ebo granites in the south margin of Altay, Xinjiang: Age, geochemistry and tectonic implcation. *Atca Petrol. Sin.* **2007**, *23*, 1909–1920, (In Chinese with English Abstract).
89. Gao, F.P.; Zhou, G.; Lei, Y.X. Early Permian granite age and geochemical characteristics in Shaerbulake of Xinjiang's Altay area and its geological significance. *Geol. Bull. China* **2010**, *29*, 1281–1293, (In Chinese with English Abstract).

90. Liu, Y.; Gao, S.; Hu, Z.; Gao, C.; Zong, K.; Wang, D. Continental and Oceanic Crust Recycling-induced Melt–Peridotite Interactions in the Trans-North China Orogen: U–Pb Dating, Hf Isotopes and Trace Elements in Zircons from Mantle Xenoliths. *J. Petrol.* **2010**, *51*, 537–571. [CrossRef]
91. Hu, Z.; Liu, Y.; Chen, L.; Zhou, L.; Li, M.; Zong, K.; Zhu, L.; Gao, S. Contrasting matrix induced elemental fractionation in NIST SRM rock glasses during laser ablation ICP-MS analysis at high spatial resolution. *J. Anal. At. Spectrom.* **2011**, *26*, 425–430. [CrossRef]
92. Liu, Y.; Hu, Z.; Zong, K.; Gao, C.; Gao, S.; Xu, J.; Chen, H. Reappraisement and refinement of zircon U-Pb isotope and trace element analyses by LA-ICP-MS. *Chin. Sci. Bull.* **2010**, *55*, 1535–1546. [CrossRef]
93. Ludwig, K.R. User's manual for isoplot 3.00, a geochronlogical toolkit for microsoft excel. *Berkeley Geochronl. Cent. Spec. Publ.* **2003**, *4*, 25–32.
94. Andersen, T. Correction of common lead in U–Pb analyses that do not report 204Pb. *Chem. Geol.* **2002**, *192*, 59–79. [CrossRef]
95. Chu, N.-C.; Taylor, R.N.; Chavagnac, V.; Nesbitt, R.W.; Boella, R.M.; Milton, J.A.; German, C.R.; Bayon, G.; Burton, K. Hf isotope ratio analysis using multi-collector inductively coupled plasma mass spectrometry: An evaluation of isobaric interference corrections. *J. Anal. At. Spectrom.* **2002**, *17*, 1567–1574. [CrossRef]
96. Blichert-Toft, J.; Albarède, F. The Lu-Hf isotope geochemistry of chondrites and the evolution of the mantle-crust system. *Earth Planet. Sci. Lett.* **1997**, *148*, 243–258. [CrossRef]
97. Griffin, W.L.; Pearson, N.J.; Belousova, E.; Jackson, S.E.; van Achterbergh, E.; O'Reilly, S.Y.; Shee, S.R. The Hf isotope composition of cratonic mantle: LAM-MC-ICPMS analysis of zircon megacrysts in kimberlites. *Geochim. Cosmochim. Acta* **2000**, *64*, 133–147. [CrossRef]
98. Li, X.H.; Long, W.G.; Li, Q.L.; Liu, Y.; Zheng, Y.F.; Yang, Y.H.; Chamberlain, K.R.; Wan, D.F.; Guo, C.H.; Wang, X.C. Penglai zircon megacrysts: A potential new working reference material for microbeam determination of Hf–O isotopes and U–Pb age. *Geostand. Geoanalytical Res.* **2010**, *34*, 117–134. [CrossRef]
99. Slodzian, G.; Lorin, J.C.; Havette, A. Effet isotopique sur les probabilités d'ionisation en émission secondaire. *C. R. Acad. Sci.* **1980**, *291*, 121–124.
100. Shimizu, N.; Hart, S.R. Isotope fractionation in secondary ion mass spectrometry. *J. Appl. Phys.* **1982**, *53*, 1303–1311. [CrossRef]
101. Wiedenbeck, M.; Hanchar, J.M.; Peck, W.H.; Sylvester, P.; Valley, J.; Whitehouse, M.; Kronz, A.; Morishita, Y.; Nasdala, L.; Fiebig, J.; et al. Further Characterisation of the 91500 Zircon Crystal. *Geostand. Geoanal. Res.* **2004**, *28*, 9–39. [CrossRef]
102. Peucat, J.; Tisserant, D.; Caby, R.; Clauer, N. Resistance of zircons to U–Pb resetting in a prograde metamorphic sequence of Caledonian age in East Greenland. *Can. J. Earth Sci.* **1985**, *22*, 330–338. [CrossRef]
103. Davis, D.W.; Paces, J.B. Time resolution of geologic events on the Keweenaw Peninsula and implications for development of the Midcontinent Rift system. *Earth Planet. Sci. Lett.* **1990**, *97*, 54–64. [CrossRef]
104. Lv, Z.-H.; Chen, J.; Zhang, H.; Tang, Y. Petrogenesis of Neoproterozoic rare metal granite-pegmatite suite in Jiangnan Orogen and its implications for rare metal mineralization of peraluminous rock in South China. *Ore Geol. Rev.* **2021**, *128*, 103923. [CrossRef]
105. Hoskin, P.W.O.; Schaltegger, U. The Composition of Zircon and Igneous and Metamorphic Petrogenesis. *Rev. Mineral. Geochem.* **2003**, *53*, 27–62. [CrossRef]
106. Li, J.; Yan, Q.; Li, P.; Ivan Jacobson, M. Formation of granitic pegmatites during orogenies: Indications from a case study of the pegmatites in China. *Ore Geol. Rev.* **2023**, *156*, 105391. [CrossRef]
107. Watson, E.; Cherniak, D. Oxygen diffusion in zircon. *Earth Planet. Sci. Lett.* **1997**, *148*, 527–544. [CrossRef]
108. Zheng, Y.-F.; Fu, B. Estimation of oxygen diffusivity from anion porosity in minerals. *Geochem. J.* **1998**, *32*, 71–89. [CrossRef]
109. Valley, J.W.; Bindeman, I.N.; Peck, W.H. Empirical calibration of oxygen isotope fractionation in zircon. *Geochim. Cosmochim. Acta* **2003**, *67*, 3257–3266. [CrossRef]
110. Zheng, Y.-F.; Wu, Y.-B.; Chen, F.-K.; Gong, B.; Li, L.; Zhao, Z.-F. Zircon U-Pb and oxygen isotope evidence for a large-scale 18O depletion event in igneous rocks during the Neoproterozoic. *Geochim. Cosmochim. Acta* **2004**, *68*, 4145–4165. [CrossRef]
111. Valley, J.W.; Chiarenzelli, J.R.; McLelland, J.M. Oxygen isotope geochemistry of zircon. *Earth Planet. Sci. Lett.* **1994**, *126*, 187–206. [CrossRef]
112. Gilliam, C.E.; Valley, J.W. Low δ18O magma, Isle of Skye, Scotland: Evidence from zircons. *Geochim. Cosmochim. Acta* **1997**, *61*, 4975–4981. [CrossRef]
113. King, E.M.; Valley, J.W.; Davis, D.W.; Edwards, G.R. Oxygen isotope ratios of Archean plutonic zircons from granite–greenstone belts of the Superior Province: Indicator of magmatic source. *Precambrian Res.* **1998**, *92*, 365–387. [CrossRef]
114. Zheng, Y. Neoproterozoic magmatic activity and global change. *Chin. Sci. Bull.* **2003**, *48*, 1639–1656. [CrossRef]
115. Zheng, Y.-F.; Fu, B.; Gong, B.; Li, L. Stable isotope geochemistry of ultrahigh pressure metamorphic rocks from the Dabie–Sulu orogen in China: Implications for geodynamics and fluid regime. *Earth-Sci. Rev.* **2003**, *62*, 105–161. [CrossRef]
116. O'Neil, J.R.; Taylor, H.P., Jr. The oxygen isotope and cation exchange chemistry of feldspars1. *Am. Mineral.* **1967**, *52*, 1414–1437.
117. Clayton, R.N.; O'Neil, J.R.; Mayeda, T.K. Oxygen isotope exchange between quartz and water. *J. Geophys. Res.* **1972**, *77*, 3057–3067. [CrossRef]
118. Jiang, Y.; Sun, M.; Zhao, G.; Yuan, C.; Xiao, W.; Xia, X.; Long, X.; Wu, F. Precambrian detrital zircons in the Early Paleozoic Chinese Altai: Their provenanceand implications for the crustal growth of central Asia. *Precambrian Res* **2011**, *189*, 140–154. [CrossRef]

119. Wang, W.; Wei, C.; Zhang, Y.; Chu, H.; Zhao, Y.; Liu, X. Age and origin of sillimanite schist from the Chinese Altai metamorphic belt: Implications for late Palaeozoic tectonic evolution of the Central Asian Orogenic Belt. *Int. Geol. Rev.* **2014**, *56*, 224–236. [CrossRef]
120. Yang, T.N.; Li, J.Y.; Zhang, J.; Hou, K.J. The Altai-Mongolia terrane in the Central Asian Orogenic Belt (CAOB): A peri-Gondwana one? Evidence from zircon U–Pb, Hf isotopes and REE abundance. *Precambrian Res.* **2011**, *187*, 79–98. [CrossRef]
121. Zhang, J.; Sun, M.; Schulmann, K.; Zhao, G.; Wu, Q.; Jiang, Y.; Guy, A.; Wang, Y. Distinct deformational history of two contrasting tectonic domains in the Chinese Altai: Their significance in understanding accretionary orogenic process. *J. Struct. Geol.* **2015**, *73*, 64–82. [CrossRef]
122. Broussolle, A.; Aguilar, C.; Min, S.; Schulmann, K.; Štípská, P.; Jiang, Y.D.; Yu, Y.; Xiao, W.; Wang, S.; Míková, J. Polycyclic Palaeozoic evolution of accretionary orogenic wedge in the southern Chinese Altai: Evidence from structural relationships and U-Pb geochronology. *Lithos* **2018**, *314*, 400–424. [CrossRef]
123. Zhang, J.; Wang, J.; Ding, R. Characteristics and U–Pb ages of zircon in meta volcanics from the Kangbutiebao Formation in the Altay orogen, Xinjiang. *Reg. Geol. China* **2000**, *19*, 281–287.
124. Chai, F.M.; Yang, F.Q.; Liu, F.; Geng, X.X.; Jiang, L.P.; Lv, S.J.; Chen, B. Geochronology and genesis of meta-felsic volcanic rocks from the Kangbutiebao formation in Chonghu'er basin on southern margin of Altay, Xinjiang. *Geol. Rev.* **2012**, *58*, 1023–1037.
125. Liu, W.; Liu, L.J.; Liu, X.J.; Shang, H.J.; Zhou, G. Age of the Early Devonian Kangbutiebao Formation along the southern Altay Mountains and its northeastern extension. *Acta Petrol. Sin.* **2010**, *26*, 387–400, (In Chinese with the English Abstract).
126. Shan, Q.; Zeng, Q.S.; Luo, Y.; Yang, W.B.; Zhang, H.; Qiu, Y.Z.; Yu, X.Y. SHRIMP U–Pb ages and petrology studies on the potassic and sodic rhyolites in Altai, North Xinjiang. *Acta Petrol. Sin.* **2011**, *27*, 3653–3665, (In Chinese with English Abstract).
127. Wan, B.; Xiao, W.; Zhang, L.; Windley, B.F.; Han, C.; Quinn, C.D. Contrasting styles of mineralization in the Chinese Altai and East Junggar, NW China: Implications for the accretionary history of the southern Altaids. *J. Geol. Soc.* **2011**, *168*, 1311–1321. [CrossRef]
128. Geng, X.; Yang, F.; Chai, F.; Liu, M.; Guo, X.; Guo, Z.; Zhang, Z. LA-ICP-MS U-Pb dating of volcanic rocks from Dadonggou ore district on southern margin of Altay in Xinjiang and its geological implications. *Miner. Depos.* **2012**, *31*, 1119–1131.
129. Guo, X.J.; Li, Y.; Kong, L.H.; Zheng, J.H.; Sun, D.Q. Geological characteristics and Metallogenesis of the Boketubayi iron-manganese deposit in Altay, Xinjiang. *Geoscience* **2015**, *29*, 1309–1318, (In Chinese with English Abstract).
130. Yang, C.; Yang, F.; Chai, F.; Wu, Y. Timing of formation of the Keketale Pb–Zn deposit, Xinjiang, Northwest China, Central Asian Orogenic Belt: Implications for the metallogeny of the South Altay Orogenic Belt. *Geol. J.* **2018**, *53*, 899–913. [CrossRef]
131. Zhao, J.Y.; Zhang, H.; Tang, Y.; Lv, Z.H. Constrains on petrogenesis and geologic implications of the keketuohai granite batholith. *Bol. Tec. Tech. Bull.* **2017**, *55*, 19–32.
132. He, D.; Dong, Y.; Xu, X.; Chen, J.; Liu, X.; Li, W.; Li, X. Geochemistry, geochronology and Hf isotope of granitoids in the Chinese Altai: Implications for Paleozoic tectonic evolution of the Central Asian Orogenic Belt. *Geosci. Front.* **2018**, *9*, 1399–1415. [CrossRef]
133. Shen, X.; Zhang, H.; Wang, Q.; Wyman, D.A.; Yang, Y. Late Devonian–Early Permian A-type granites in the southern Altay Range, Northwest China: Petrogenesis and implications for tectonic setting of "A2-type" granites. *J. Asian Earth Sci.* **2011**, *42*, 986–1007. [CrossRef]
134. Zhang, C.; Liu, D.; Luo, Q.; Liu, L.; Zhang, Y.; Zhu, D.; Wang, P.; Dai, Q. An evolving tectonic environment of Late Carboniferous to Early Permian granitic plutons in the Chinese Altai and Eastern Junggar terranes, Central Asian Orogenic Belt, NW China. *J. Asian Earth Sci.* **2018**, *159*, 185–208. [CrossRef]
135. Kong, X.; Zhang, C.; Liu, D.; Jiang, S.; Luo, Q.; Zeng, J.; Liu, L.; Luo, L.; Shao, H.; Liu, D.; et al. Disequilibrium partial melting of metasediments in subduction zones: Evidence from O-Nd-Hf isotopes and trace elements in S-type granites of the Chinese Altai. *Lithosphere* **2018**, *11*, 149–168. [CrossRef]
136. Zhang, C.; Liu, D.; Zeng, J.; Jiang, S.; Luo, Q.; Kong, X.; Yang, W.; Liu, L. Nd-O-Hf isotopic decoupling in S-type granites: Implications for ridge subduction. *Lithos* **2019**, *332*, 261–273. [CrossRef]
137. Deschamps, F.; Duchêne, S.; de Sigoyer, J.; Bosse, V.; Benoit, M.; Olivier, V. Coevalmantle-derived and crust-derived magmas forming two neighbouring plutons inthe Songpan Ganze Accretionary Orogenic Wedge (SW China). *J. Petrol.* **2017**, *58*, 2221–2256. [CrossRef]
138. Ma, S.C.; Wang, D.H.; Liu, S.B.; Sun, Y.; Guo, W.M.; Dai, H.Z.; Liu, L.J.; Li, C. Mineralchemistry of micas from Ke'eryin pegmatite type lithium orefield in western Sichuanand its indication for rare metal mineralization and prospecting. *Miner. Depos.* **2019**, *38*, 877–897, (In Chinese with English Abstract).
139. Li, X.F.; Tian, S.H.; Wang, D.H.; Zhang, H.J.; Zhang, Y.J.; Fu, X.D.; Hao, X.F.; Hou, K.J.; Yu, Y.; Wang, H. Genetic relationship betweenpegmatite and granite inJiajika lithiumdeposit in western Sichuan: Evidence from zircon U-Pb dating, Hf-O isotope and geo-chemistry. *Miner. Depos.* **2020**, *39*, 273–304, (In Chinese with English Abstract).
140. Wedepohl, K.H. The composition of the continental crust. *Geochim. Cosmochim. Acta* **1995**, *59*, 1217–1232. [CrossRef]
141. Evensen, J.M.; London, D. Experimental silicate mineral/melt partition coefficients for beryllium, and the beryllium cycle from migmatite to pegmatite. *Geochim. Cosmochim. Acta* **2002**, *66*, 2239–2265. [CrossRef]
142. London, D. Reading pegmatites: What beryl says. *Rocks Min.* **2015**, *90*, 138–149. [CrossRef]
143. Zhang, Z.; Yan, S.; Chen, B.; Zhou, G.; He, Y.; Chai, F.; He, L.; Wan, Y. SHRIMP zircon U-Pb dating for subduction-related granitic rocks in the northern part of east Jungaar, Xinjiang. *Chin. Sci. Bull.* **2006**, *51*, 952–962. [CrossRef]

144. Li, Z.X.; Li, X.H.; Chung, S.L.; Lo, C.H.; Xu, X.S.; Li, W.X. Magmatic switch-on and switch-off along the South China continental margin since the Permian: Transition from an Andean-type to a Western Pacific-type plate boundary. *Tectonophysics* **2012**, *532*, 271–290. [CrossRef]
145. Zhang, C.L.; Santosh, M.; Zou, H.B.; Xu, Y.G.; Zhou, G.; Dong, Y.G.; Ding, R.-F.; Wang, H.Y. Revisiting the "Irtish tectonic belt": Implications for the Paleozoic tectonic evolution of the Altai orogen. *J. Asian Earth Sci.* **2012**, *52*, 117–133. [CrossRef]
146. Wan, B.; Xiao, W.; Windley, B.F.; Yuan, C. Permian hornblende gabbros in the Chinese Altai from a subduction-related hydrous parent magma, not from the Tarim mantle plume. *Lithosphere* **2013**, *5*, 290–299. [CrossRef]
147. Zhang, Y.; Chen, J.L.; Bai, J.K.; Tang, Z. LA-ICP-MS zircon U-Pb dating of gneissic granitic intrusive mass in Wuqiagou on the southern margin of Altay Orogenic Belt andits geological significance. *Northwest. Geol.* **2015**, *48*, 127–139, (In Chinese with English Abstract).
148. Tong, Y.; Wang, T.; Kovach, V.P.; Hong, D.W.; Dai, Y.J.; Han, B.F. Age and origin of Takeshiken postorogenic alkali-rich intrusive rocks in southern Altai, near the Mongolian border in China and its implication for continental growth. *Acta Petrol. Sin.* **2006**, *22*, 1267–1278.
149. Zhang, C.-L.; Li, Z.-X.; Li, X.-H.; Xu, Y.-G.; Zhou, G.; Ye, H.-M. A Permian large igneous province in Tarim and Central Asian orogenic belt, NW China: Results of a ca. 275 Ma mantle plume? *GSA Bull.* **2010**, *122*, 2020–2040. [CrossRef]
150. Lin, Z.; Yuan, C.; Zhang, Y.; Sun, M.; Long, X.; Wang, X.; Huang, Z.; Chen, Z. Petrogenesis and geodynamic implications of two episodes of Permian and Triassic high-silica granitoids in the Chinese Altai, Central Asian Orogenic Belt. *J. Asian Earth Sci.* **2019**, *184*, 103978. [CrossRef]
151. Pearce, J.A.; Harris, N.B.W.; Tindle, A.G. Trace Element Discrimination Diagrams for the Tectonic Interpretation of Granitic Rocks. *J. Petrol.* **1984**, *25*, 956–983. [CrossRef]
152. Tong, Y.; Wang, T.; Hong, D.W.; Dai, Y.J.; Han, B.F.; Liu, X.M. Ages and origin of the early Devonian granites from the north part of Chinese Altai Mountains and its tectonic implcations. *Atca Petrol. Sin.* **2007**, *23*, 1933–1944, (In Chinese with English Abstract).
153. Baker, D.R. The escape of pegmatite dykes from granitic plutons: Constraints from new models of viscosity and dike propagation. *Can Miner.* **1998**, *36*, 255–263.
154. Sengör, A.M.C.; Natal'in, B.A. Turkic-type orogeny and its role in the making of the continental crust. *Annu. Rev. Earth Planet. Sci.* **1996**, *24*, 263–337. [CrossRef]
155. He, G.Q.; Han, B.F.; Yue, Y.J.; Wang, J.H. Tectonic division and crustal evolutionof Altay orogenic belt in China. *Geosci. Xinjiang* **1990**, *2*, 9–20, (In Chinese with English Abstract).
156. Li, H.J.; He, G.Q.; Wu, T.R.; Wu, B. Confirmation of Altai-Mongolia microcontinent and its implications. *Acta Petrol. Sin.* **2006**, *22*, 1369–1379. (In Chinese)
157. Xiao, W.; Windley, B.F.; Sun, S.; Li, J.; Huang, B.; Han, C.; Yuan, C.; Sun, M.; Chen, H. A tale of amalgamation of three Permo-Triassic collage systems in Central Asia: Oroclines, sutures, and terminal accretion. *Annu. Rev. Earth Planet. Sci.* **2015**, *43*, 477–507. [CrossRef]
158. Wang, Z.; Wu, J.; Lu, X.; Liu, C.; Zhang, J. Polycyclic tectonic evolution and metallogeny of the Tianshan Mountains. *Beijing Sci. Press* **1990**, *29*, 37.
159. Windley, B.F.; Allen, M.B.; Zhang, C.; Zhao, Z.Y.; Wang, G.R. Paleozoic accretion and Cenozoic redeformation of the Chinese Tien Shan Range, central Asia. *Geology* **1990**, *18*, 128–131. [CrossRef]
160. Allen, M.B.; Windley, B.F.; Zhang, C. Palaeozoic collisional tectonics and magmatism of the Chinese Tien Shan, central Asia. *Tectonophysics* **1993**, *220*, 89–115. [CrossRef]
161. Gao, J.; He, G.; Li, M.; Xiao, X.; Tang, Y.; Wang, J.; Zhao, M. The mineralogy, petrology, metamorphic PTDt trajectory and exhumation mechanism of blueschists, south Tianshan, northwestern China. *Tectonophysics* **1995**, *250*, 151–168. [CrossRef]
162. Sun, S.; Li, J.L.; Lin, J.L.; Wang, Q.C.; Chen, H.H. Indosinides in China and the consumption of Eastern Paleotethys. In *Symposium Controversies in Modern Geology*; The Institute of Geology and Geophysics, Chinese Academy of Sciences (IGGCAS): Beijing, China, 1991; pp. 363–384.
163. Li, Y.; Sun, L.; Wu, H.; Wang, G.; Peng, G. Permo-carboniferous radiolaria from the wupatarkan group, west terminal of chinese south tianshan. *Chin. J. Geol.* **2005**, *40*, 220–226.
164. Xiao, W.; Windley, B.; Yan, Q.; Qin, K.; Chen, H.; Yuan, C.; Sun, M.; Li, J.; Sun, S. SHRIMP zircon age of the Aermantai ophiolite in the North Xinjiang area, China and its tectonic implications. *Acta Geol. Sin.* **2006**, *80*, 32–36.
165. Xiao, W. The unique Carboniferous-early Permian tectonic-metallogenic framework of Northern Xinjiang (NW China): Constraints for the tectonics of the southern Paleo Asian Domain. *Acta Petrol. Sin.* **2006**, *22*, 1062–1076.
166. Vladimirov, A.G.; Vystavnoi, S.A.; Titov, A.V.; Rudnev, S.N.; Dergachev, V.B.; Annikova, I.Y.; Tikunov, Y.V. Petrology of the Early Mesozoic rare-metal granitesof the southern Gorny Altai. *Geol. Geofiz. Russ. Geol. Geophys.* **1998**, *39*, 909–924.
167. Altukhov, E.N.; Altukhov, E.E.; Vashurin, A.I.; Usova, T.Y. *Fundamentals of Rare-Metal Metallogeny*; IMGRE: Russia, Moscow, 2005; pp. 1–20. (In Russian)
168. Martin, R.F.; De Vito, C. The patterns of enrichment in felsic pegmatites ultimately depend on tectonic setting. *Can. Mineral.* **2005**, *43*, 2027–2048. [CrossRef]
169. Gusev, G.S.; Gushchin, A.V.; Mezhelovskiy, N.V.; Kilipko, V.A. Two types of rare metal mineralization in territory of Russia: Geodynamic models of forming. *Razvedka Okhrana Nedr.* **2012**, *2*, 38–42.

170. Vladimirov, A.G.; Izokh, A.E.; Polyakov, G.V.; Babin, G.A.; Mekhonoshin, A.S.; Kruk, N.N.; Khlestov, V.V.; Khromykh, S.V.; Travin, A.V.; Yudin, D.S.; et al. Gabbro–granite intrusive series and theirindicator importance for geodynamic reconstructions. *Petrology* **2013**, *21*, 158–180. [CrossRef]
171. Jahn, B.M.; Wu, F.; Chen, B. Granitoids of the Central Asian orogenic belt andcontinental growth in the Phanerozoic. *Trans. R. Soc. Edinb. Earth Sci.* **2000**, *91*, 181–193.
172. Jahn, B.M.; Wu, F.Y.; Chen, B. Massive granitoid generation in Central Asia: Ndisotope evidence and implication for continental growth in the Phanerozoic. *Episodes* **2000**, *23*, 82–92. [CrossRef] [PubMed]
173. Li, P.; Sun, M.; Rosenbaum, G.; Jourdan, F.; Li, S.; Cai, K. Late Paleozoic closure of the Ob-Zaisan Ocean along the Irtysh shear zone (NW China): Implications for arc amalgamation and oroclinal bending in the Central Asian orogenic belt. *GSA Bull.* **2017**, *129*, 547–569. [CrossRef]
174. Hu, W.; Li, P.; Rosenbaum, G.; Liu, J.; Jourdan, F.; Jiang, Y.; Wu, D.; Zhang, J.; Yuan, C.; Sun, M. Structural evolution of the eastern segment of the Irtysh Shear Zone: Implications for the collision between the East Junggar Terrane and the Chinese Altai Orogen (northwestern China). *J. Struct. Geol.* **2020**, *139*, 104–126. [CrossRef]
175. Li, P.; Sun, M.; Rosenbaum, G.; Cai, K.; Yu, Y. Structural evolution of the Irtysh shear zone (north-western China) and implications for the amalgamation of arc systems in the Central Asian orogenic belt. *J. Struct. Geol.* **2015**, *80*, 142–156. [CrossRef]
176. Li, Z.; Yang, X.; Li, Y.; Santosh, M.; Chen, H.; Xiao, W. Late Paleozoic tectono-metamorphic evolution ofthe Altai segment of the Central Asian orogenic belt: Constraints from metamorphic P-T pseudosection and zirconU-Pb dating of ultra-high-temperature granulite. *Lithos* **2014**, *204*, 83–96. [CrossRef]
177. Pearce, J.A.; Bender, J.F.; Delong, S.E.; Kidd, W.S.F.; Low, P.J.; Guner, Y.; Sargolu, F.; Yilmaz, Y.; Moorbath, S.; Mitchell, J.G. Genesis of collision volcanism ineastern Anatolia, Turkey. *J. Volcanol. Geotherm. Res.* **1990**, *44*, 189–229. [CrossRef]
178. Turner, S.; Sandiford, M.; Foden, J. Some geodynamic and compositional constraints on 'postorogenic' magmatism. *Geology* **1992**, *20*, 931–934. [CrossRef]
179. Kay, R.W.; Mahlburg Kay, S. Delamination and delamination magmatism. *Tectonophysics* **1993**, *219*, 177–189. [CrossRef]
180. Bird, P. Continental delamination and the Colorado Plateau. *J. Geophys. Res.* **1979**, *84*, 7561–7571. [CrossRef]
181. Houseman, G.A.; McKenzie, D.P.; Molnar, P. Convective instability of a thickened boundary layer and its relevance for the thermal evolution of continental convergent belts. *J. Geophys. Res. Solid Earth* **1981**, *86*, 6115–6132. [CrossRef]
182. Liégeois, J.-P.; Navez, J.; Hertogen, J.; Black, R. Contrasting origin of post-collisional high-K calc-alkaline and shoshonitic versus alkaline and peralkaline granitoids. The use of sliding normalization. *Lithos* **1998**, *45*, 1–28. [CrossRef]
183. Bonin, B. Do coeval mafic and felsic magmas in post-collisional to within-plate regimes necessarily imply two contrasting, mantle and crustal, sources? A review. *Lithos* **2004**, *78*, 1–24. [CrossRef]
184. Duggen, S.; Hoernle, K.; van Den Bogaard, P.; Garbe-Schönberg, D. Post-Collisional Transition from Subduction- to Intraplate-type Magmatism in the Westernmost Mediterranean: Evidence for Continental-Edge Delamination of Subcontinental Lithosphere. *J. Petrol.* **2005**, *46*, 1155–1201. [CrossRef]
185. Zhao, Z.F.; Zheng, Y.F.; Wei, C.S.; Wu, Y.B. Post-collisional granitoids from the Dabie orogen in China: Zircon U–Pb age, element and O isotope evidence for recycling of subducted continental crust. *Lithos* **2007**, *93*, 248–272. [CrossRef]